8-20-2020

EMIC Waves in the Earth's Inner Magnetosphere as a Function of Solar Wind Structures During Solar Maximum

Konstantin V. Gamayunov

Mark J. Engebretson

Scot R. Elkington

JGR Space Physics

RESEARCH ARTICLE
10.1029/2020JA027990

EMIC Waves in the Earth's Inner Magnetosphere as a Function of Solar Wind Structures During Solar Maximum

Konstantin V. Gamayunov[1], **Mark J. Engebretson**[2], **and Scot R. Elkington**[3]

[1]Department of Aerospace, Physics and Space Sciences, Florida Institute of Technology, Melbourne, FL, USA, [2]Department of Physics, Augsburg University, Minneapolis, MN, USA, [3]Laboratory for Atmospheric and Space Physics, University of Colorado Boulder, Boulder, CO, USA

Key Points:

- General statistics of EMIC waves in the Earth's inner magnetosphere during CME, HSS, and QSW conditions are presented
- Geomagnetic contexts of EMIC wave events during CME, HSS, and QSW conditions are quantified
- Global spatial and frequency distributions of EMIC waves during CME, HSS, and QSW conditions are presented

Correspondence to:
K. V. Gamayunov,
kgamayunov@fit.edu

Citation:
Gamayunov, K. V., Engebretson, M. J., & Elkington, S. R. (2020). EMIC waves in the Earth's inner magnetosphere as a function of solar wind structures during solar maximum. *Journal of Geophysical Research: Space Physics*, *125*, e2020JA027990. https://doi.org/10.1029/2020JA027990

Received 9 MAR 2020
Accepted 22 JUN 2020
Accepted article online 20 AUG 2020

Abstract Here we analyze the statistics of electromagnetic ion cyclotron (EMIC) waves observed in the Earth's inner magnetosphere during coronal mass ejection (CME), high-speed stream (HSS), and quiet solar wind (QSW) conditions in the upstream solar wind (SW). For our analysis we use the EMIC wave observations by the two Van Allen Probes during their first magnetic local time (MLT) revolution. The major results of our analysis are as follows: (1) Criteria to identify the HSS, CME, and QSW conditions in the SW are formulated. (2) 54%, 36%, and 10% of EMIC wave events are observed during CME, HSS, and QSW, respectively. (3) 12% of events are closely associated with the fast growth of magnetospheric compression, among which 76%, 24%, and 0% are observed during CME, HSS, and QSW, respectively. (4) A majority of the QSW, HSS-driven, and CME-driven events is observed in the 9–12, 12–24, and 8–24 hr MLT sectors, respectively. (5) CME-driven events are distributed along all L shells, whereas the majority of the HSS-driven and QSW events are confined to $L > 3.5$. (6) The fractions of events during CME and HSS have a maximum in the near-equatorial region, whereas the fractions of the QSW events have a minimum there. (7) Independent of the SW driver, no strong events are observed below the local O^+ gyrofrequency, whereas 65–70% and 30–35% of events are observed between the O^+ and He^+ gyrofrequencies and above the He^+ gyrofrequency, respectively.

1. Introduction

Electromagnetic ion cyclotron (EMIC) waves have frequencies below the proton gyrofrequency, and these waves are commonly observed in Earth's magnetosphere (e.g., Anderson et al., 1992a, 1992b; Clausen et al., 2011; Fraser et al., 2010; Gamayunov et al., 2018; Halford et al., 2010; Min et al., 2012; Saikin et al., 2015; Tetrick et al., 2017; Usanova et al., 2012). EMIC waves strongly affect the ring current (RC) protons (e.g., Gonzalez et al., 1989) and heavy ions (e.g., Thorne & Horne, 1994, 1997), thermal electrons (e.g., Cornwall et al., 1971) and ions (e.g., Anderson & Fuselier, 1994), and radiation belt (RB) relativistic electrons (e.g., Gamayunov & Khazanov, 2007; Lorentzen et al., 2000; Mourenas et al., 2016; Sandanger et al., 2007), leading to nonadiabatic particle heating and/or pitch angle scattering in the eV-MeV energy range. The upstream solar wind (SW) activity, on the other hand, is ultimately responsible for the physical processes and geomagnetic activity occurring in the magnetosphere. For example, the large-scale convective motion of magnetospheric plasma is driven by dayside magnetic reconnection between the interplanetary magnetic field (IMF) and the magnetospheric field (e.g., Dungey, 1961; Ridley et al., 1997; Saunders et al., 1992) during periods when the IMF is oriented southward and also during periods of northward IMF via reconnection at high latitudes (e.g., Fuselier et al., 2000; Trattner et al., 2004). Reconnection provides an efficient means of transmitting energy from the SW into the magnetosphere, driving periodic releases of magnetic flux and plasma from the tail of magnetosphere in the form of substorms (e.g., Ge et al., 2011; Russell & McPherron, 1973; Wiltberger et al., 2015). The earthward plasma flows resulting from both substorms and the large-scale convective motion can contribute to the energetic particle populations forming the RC (Tsurutani & Gonzalez, 1997; Wygant et al., 1998), driving the depressions in magnetic field strength on the Earth's surface that characterize geomagnetic storms. The earthward flows may also contribute to the plasma temperature anisotropies that result in the generation of EMIC waves and whistler mode chorus waves in the inner magnetosphere (e.g., Golden et al., 2012; McCollough et al., 2009, 2010). The SW likewise contributes to low-frequency (~mHz) magnetohydrodynamic waves via Kelvin-Helmholtz instabilities on the magnetospheric flanks (Claudepierre et al., 2008; Dungey, 1955; Kivelson & Pu, 1984), through direct driving via pressure variations in the SW (Claudepierre et al., 2009, 2010; Sibeck, Baumjohann, et al., 1989; Sibeck, Lopez, et al., 1989) and via fluctuations in the IMF.

Activity in the SW may be broadly characterized as driven by the high-speed streams (HSSs) associated with corotating interaction regions (CIRs) (e.g., Tsurutani et al., 1995) or via transient events associated with coronal mass ejections (CMEs) (e.g., Burlaga et al., 1982, 1990; Groth et al., 2000). The former might be characterized by an initial increase in the SW density, followed by a steadily increasing SW speed and strong Alfvénic fluctuations in the IMF. The CME events, on the other hand, may be characterized by shock-like discontinuities in the density and velocity of the SW and IMF (e.g., Hudson et al., 2015) and may exhibit subsequent internal structures such as those associated with magnetic flux ropes and/or ejecta (e.g., Baker et al., 1998; Clemmons et al., 2000). The upstream SW structures such as CMEs and HSSs control the EMIC wave generation, the wave global spatial distribution and occurrence rates, and also affect the different local characteristics of the generated EMIC waves. The various manifestations of geomagnetic activity, for example, RC, magnetospheric convection, aurora and particle precipitation, and RBs depend on whether geomagnetic activity is driven by CME or HSS (e.g., Borovsky & Denton, 2006, and references therein). So it is expected that spatial distributions, occurrence rates, and different characteristics of EMIC waves generated under different SW drivers will be also different. Currently, however, there are no systematic studies of similarities and/or differences in the EMIC wave spatial distributions and the wave occurrence rates and their characteristics observed under different SW drivers, despite a number of both statistical and case studies of EMIC waves. There is probably only one exception where numerous studies have analyzed the effect of the upstream SW dynamic pressure on EMIC wave occurrence rates (e.g., Park et al., 2016; Saikin et al., 2016; Usanova et al., 2012, and references therein).

In this work we systematically analyze the statistics of EMIC waves observed in the Earth's inner magnetosphere during CME, HSS, and quiet solar wind (QSW) conditions in the upstream SW. To our knowledge, such an analysis for EMIC waves is done here for the first time. This paper is organized as follows. In section 2, we describe the Van Allen Probes data to be used in our study. In section 3.1, we formulate the quantitative criteria used to identify the HSS, CME, and QSW conditions in the upstream SW. In section 3.2, the statistics of EMIC waves during the CME, HSS, and QSW events are presented and discussed. In section 3.3, we first formulate the quantitative criteria used here to identify the EMIC wave events closely associated with the fast growth of magnetospheric compression, and then present and analyze the statistics of those EMIC wave events during the CME, HSS, and QSW conditions in the upstream SW. In sections 3.4–3.10, the SYM/H index, Kp index, AE index, magnetic local time (MLT), L shell, magnetic latitude (MLAT), and frequency statistics of EMIC waves observed during the CME, HSS, and QSW conditions are presented and analyzed, respectively. Finally, in section 4 we summarize the major results and conclusions of our study.

2. Magnetic Field Data and EMIC Waves to be Used

The magnetic field data in the inner magnetosphere are taken from the Electric and Magnetic Field Instrument Suite and Integrated Science (EMFISIS) observations (Kletzing et al., 2013) onboard the two Van Allen Probes spacecraft. The two Van Allen Probes (Kessel et al., 2013; Mauk et al., 2013) were launched together on 30 August 2012 into almost the same highly elliptical, low-inclination (~10°) orbits, with a perigee of 1.1 Earth radii (R_E), apogee of 5.8 R_E and an orbital period of ~9 hr. While the inclination of the probes is fixed, their magnetic latitudes vary in the range of about MLAT = ±20° due to the tilt of the geomagnetic axis and precession of the probes' perigee-apogee lines, which precess in MLT at a rate of ~210°/year. Here we analyze the EMFISIS observations during the time period from 1 October 2012 to 7 June 2014. During this period both spacecraft completed their first pass through all MLTs.

To identify the EMIC wave events in the EMFISIS data, we first specify the power background level $W_{\mathrm{bg}} = 10^{-3}$ nT^2/Hz. Then, magnetic fluctuations in the EMIC wave frequency range (0.1–5 Hz) with their power continuously above W_{bg} are counted as a separate EMIC wave event. For each EMIC wave event the following information is recorded: event date, start time and end time, duration, Dst, SYM/H, Kp, AE, starting and ending MLTs, starting and ending L shells, starting and ending MLATs, minimum and maximum frequencies, average proton gyrofrequency, and peak wave power perpendicular and parallel to the local magnetic field and in the radial and azimuthal directions (calculated after rotating the magnetic field data

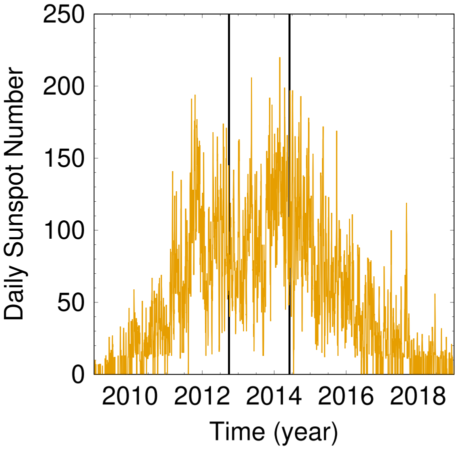

Figure 1. Daily sunspot numbers during the years of 2009–2019 (solar cycle 24). The two vertical black lines mark the time period from 1 October 2012 to 7 June 2014 during which the two Van Allen Probes completed their first pass through all local times. All the strongest EMIC wave events (with peak power greater than 10^{-1} nT^2/Hz) observed by both probes during their first MLT revolution are analyzed here.

into local mean field coordinates). The peak wave power values are the peaks of the FFT spectrum calculated using the time range from the beginning to the end of an EMIC wave event. Because the wave power usually increases gradually at the beginning, usually decreases gradually at the end, and often varies during each event, the calculated peak values are usually lower than power values calculated using a smaller time interval centered on an EMIC wave event maximum.

Among all the EMIC wave events identified during the first MLT revolution of Van Allen Probes, only the strongest events with peak wave power greater than threshold $W_{\mathrm{th}} = 10^{-1}$ nT^2/Hz are analyzed. This totals to 211 strongest EMIC wave events. The duration of the strongest events is in the range of 2–186 min, and events are observed in the following spatial and frequency ranges: MLT = 0–24 hr, L = 2.4–6.5, $-20^\circ \lesssim$ MLAT $\lesssim 17^\circ$, and $F/F_{\mathrm{O}^+} \approx 1$–10, where F and F_{O^+} are the EMIC wave frequency and the local O$^+$ gyrofrequency, respectively. Figure 1 shows the daily sunspot numbers during the years of 2009–2019, where the two vertical black lines mark the time period during which the strongest EMIC wave events are analyzed here. As follows from Figure 1, the first MLT revolution of the Van Allen Probes takes place during solar maximum of the 24th solar cycle. So all the results presented in this study are obtained during solar maximum.

3. Results

3.1. Criteria to Identify the HSS, CME, and QSW Events

As the geomagnetic response varies between the HSS, CME, and QSW categories of the SW activity (e.g., Bingham et al., 2019; Ogawa et al., 2019; Shen et al., 2017), for statistical studies of EMIC wave events, it is important to have a systematic way of identifying the associated state of the SW. To identify the HSS, CME, and QSW conditions in the upstream SW we analyze the magnitude ($|B|$) and north-south component (B_z) of the IMF, the SW speed (V_{sw}), and the SW proton density (N_{sw}) preceding and during each EMIC wave event analyzed in this study. Here we use the 5-min time resolution OMNI data, and all the SW data are propagated in time from the upstream point of observation to the nose of the Earth's bow shock. According to the work by Borovsky et al. (1998), the transport time of the SW material from the dayside magnetopause to the midnight (MLT = 24 hr) geosynchronous plasma sheet is $T_{24} = 0$–7 hr (on average ∼4 hr), and the respective transport time to the dayside (MLT = 12 hr) geosynchronous plasma sheet is $T_{12} = 11$–18 hr (on average ∼15 hr). In order to include in our analysis the largest transport time for the SW material from MLT = 24 hr to MLT = 12 hr, and also to take into account the smallest time delay between the dayside magnetopause and the midnight geosynchronous plasma sheet, below we adopt $T_{24} = 0$ and $T_{12} = 18$ hr. Taking T_{EMIC} as the universal time (UT) of the end of an analyzed EMIC wave event, we first produce the plots of $|B|$,B_z, V_{sw}, and N_{sw} during the time interval T_1–T_2, where $T_1 = T_{\mathrm{EMIC}} - T_{12}$ and $T_2 = T_{\mathrm{EMIC}} - T_{24}$, for all the EMIC wave events analyzed here. Then the criteria formulated below in sections 3.1.1–3.1.3 are used to analyze the produced plots in order to classify all EMIC wave events according to the preceding SW conditions. The criteria presented below were formulated after our analysis of 211 EMIC wave events with peak power $\geq 10^{-1}$ nT^2/Hz that were observed by the two Van Allen Probes during their first pass through all MLTs. The resulting quantitative criteria are based on common knowledge about HSS, CME, and QSW (e.g., Borovsky & Denton, 2006, and references therein) combined with an additional requirement that as many observed EMIC wave events as possible are categorized in the HSS, CME, and QSW categories. Among the 211 EMIC wave events analyzed here, only one wave event was left uncategorized.

3.1.1. HSS Events

The HSS events are associated with both the recurrent (with 27-day recurrence) CIRs and nonrecurrent interaction regions (IRs) (e.g., Borovsky & Denton, 2006, and references therein). In the HSS criteria formulated below, however, we do not separate the above two cases and so do not control whether or not the HSS events are associated with CIRs and/or IRs. Here we identify the upstream SW conditions as an HSS event if $V_{\mathrm{sw}} \gtrsim 400$ km/s at any time during the analyzed time interval T_1–T_2, and in addition any of the following alternatives takes place:

Table 1
Categorization of the Strongest EMIC Wave Events Observed by the Two Van Allen Probes During 1 October 2012 Through 7 June 2014 According to the Upstream SW Structures Before and During the Events

	CME in SW	HSS in SW	QSW	Total[a]
Number of events	113	76	21	210
Percentage of events	54	36	10	100

[a] One EMIC wave event was left uncategorized and is not included here.

1. V_{sw} grows from the slow SW level ($\lesssim 400$ km/s), and peaks of $N_{sw} > 10\ \mathrm{cm}^{-3}$, $|B| > 10$ nT, and oscillations of B_z with $|B_z| \gtrsim 10$ nT are observed. In this case, CIR and/or IR are/is observed, and an example of OMNI data during the growth phase of an HSS event is shown in Figure A1.
2. V_{sw} has a quasi-plateau at the fast SW level ($\sim$ 500–800 km/s), and oscillations in V_{sw} with $\gtrsim 20$ km/s peak-to-peak along with oscillations in $|B|$ with $\gtrsim 3$ nT peak-to-peak and/or B_z with $\gtrsim 3$ nT peak-to-peak are observed. An example of OMNI data during the quasi-plateau phase of an HSS event is shown in Figure A2.
3. V_{sw} decreases from the fast to slow SW level, and oscillations in V_{sw} with $\gtrsim 20$ km/s peak-to-peak along with oscillations in $|B|$ with $\gtrsim 3$ nT peak-to-peak and/or B_z with $\gtrsim 3$ nT peak-to-peak are observed. An example of OMNI data during the declining phase of an HSS event is shown in Figure A3.
4. Any combination of the above three scenarios is observed.

3.1.2. CME Events

The CME events consist of an interplanetary shock, a sheath of compressed SW, and ejecta and/or a magnetic cloud (e.g., Borovsky & Denton, 2006, and references therein). Here we identify the SW conditions as a CME event if any of the following alternatives takes place:

1. A shock-like increase in V_{sw}, N_{sw}, and $|B|$ is observed. In this case, an interplanetary shock is observed, and an example of OMNI data during the shock phase of a CME event is shown in Figure A4.
2. Smooth and slow (over ~1 day) growth and/or decrease of $|B|$ from about a few nT up to $|B| \gtrsim 10$ nT and also a smooth change ("rotation") of B_z are observed. In this case, a magnetic cloud is observed, and an example of OMNI data during the magnetic cloud phase of a CME event is shown in Figure A5.
3. Smooth and slow (over ~1 day) growth and/or decrease of N_{sw} from about a few cm^{-3} up to $N_{sw} \gtrsim 10\ \mathrm{cm}^{-3}$ are/is observed. In this case, ejecta are observed, and an example of OMNI data during the ejecta phase of a CME event is shown in Figure A6.
4. Any combination of the above three scenarios is observed.

3.1.3. QSW Events

In this study we identify the SW conditions as a QSW event if the following conditions are satisfied:

1. $V_{sw} \lesssim 400$ km/s is observed during 100% of time, and all conditions in Items 1–3 from section 3.1.2 are not satisfied. An example of OMNI data during a QSW event is shown in Figure A7.

3.2. Statistics of EMIC Waves During CME, HSS, and QSW

To categorize the strongest EMIC wave events that were observed by the two Van Allen Probes during their first pass through all MLTs, the criteria formulated in section 3.1 are used. The results of our categorization are summarized in Table 1. Note that among the 211 EMIC wave events analyzed here, one event was left uncategorized, and we did not include it in Table 1. The majority of EMIC wave events (~54%) are observed during CME conditions in the upstream SW, while only ~36% of EMIC wave events are observed during HSSs. This is a quite expected result because the CME occurrence rates are greatest during solar maximum, and the HSS events associated with the 27-day recurring CIRs generally occur in the late declining phase of the solar cycle, while some exceptions to these general trends are also reported (e.g., Borovsky & Denton, 2006, and references therein). Because all the EMIC wave events in Table 1 are observed during solar maximum, the analyzed period of time is dominated by the CME events. Note, however, that the total numbers of EMIC wave events observed during different SW drivers depend not only on the probability of those drivers to take place. The number of EMIC wave events under particular SW driver also depends on the EMIC wave occurrence rate during this SW driver. It is obvious, at the same time, that the EMIC wave occurrence rates during different SW drivers are not necessarily the same. During QSW conditions in the upstream SW, a quite large percentage of strong EMIC wave events (~10%) is also observed.

3.3. Statistics of EMIC Waves Closely Associated With the Fast Growth of Magnetospheric Compression

It would be informative to identify in our database the EMIC wave events that are associated with magnetospheric compression, because it was previously demonstrated that compression of the dayside Earth's magnetosphere by the upstream SW dynamic pressure may correlate with EMIC wave generation (e.g., Park et al., 2016; Saikin et al., 2016; Usanova et al., 2012, and references therein). Earth's dayside magnetosphere is always compressed by the upstream SW flow, and this permanent compression exists even during QSW, and so during quiet geomagnetic conditions when both the SYM/H and Dst indices are around zero. The QSW compression of the magnetosphere causes a permanent dayside to nightside asymmetry of the DC magnetic field. The magnetic field asymmetry, on the other hand, affects the RC ion distribution functions in such a way that distribution functions become more unstable during the ion drift from the nightside magnetosphere toward the dayside magnetosphere. This “passive” manifestation of a quasi-static magnetospheric compression, that is, a manifestation which is not related to any active processes in the upstream SW, may routinely lead to generation of EMIC waves in the dayside magnetosphere (e.g., Park et al., 2016; Usanova et al., 2012). In this section, however, we do not analyze the effects of a permanent, slowly varying, compression of the dayside magnetosphere on EMIC wave generation (these effects will be discussed separately in section 3.7). Here we identify and discuss only those EMIC wave events that are driven by the effects of fast (see the next paragraph for quantification of “fast”) growth of magnetospheric compression. Hereafter, we call those events EMIC wave events closely associated with the fast growth of magnetospheric compression.

Analyzing the 5-min SYM/H index during the time interval from ∼1 hr before the onset through the end of each EMIC wave event, we identify an EMIC wave event as closely associated with the fast growth of magnetospheric compression if the following two conditions are satisfied:

1. SYM/H grows at any time during the analyzed time interval.
2. The maximum of the SYM/H index is $\mathrm{SYM/H_{max}} > 10$ nT inside the analyzed time interval.

The perturbations of Earth's magnetic field caused by compression of the dayside magnetopause propagate through magnetosphere at the Alfvén speed. So it takes less than ∼10 min for the magnetic perturbations to spread over ∼20 R_E. However, the time interval ∼1 hr is intentionally taken that large in the above two conditions to make sure that we do not miss any EMIC wave events closely associated with the fast growth of magnetospheric compression. The second condition guarantees that the dayside magnetopause current (the Chapman-Ferraro current) dominates the other magnetospheric currents, and so the effects of magnetospheric compression also dominate. The SYM/H index and Dst index are close to each other, and the high-resolution SYM/H index is usually used as a de facto high-resolution Dst index (e.g., Wanliss & Showalter, 2006, and references therein). So both the high-resolution (up to 1-min) SYM/H index and the 1-hr resolution Dst index may be used to characterize the magnetospheric compression. Given the fact that a typical difference between the above two indices is $\lesssim 10$ nT (e.g., Wanliss & Showalter, 2006, and references therein), the threshold for $\mathrm{SYM/H_{max}}$ in the above second condition is taken to be 10 nT. Finally, note that analysis of the SYM/H index is more reliable compared to an analysis of the SW dynamic pressure used in all previous works (e.g., Usanova et al., 2012, and references therein) because the SYM/H index characterizes the conditions inside the magnetosphere, but not in the SW upstream of the Earth's bow shock as the SW dynamic pressure does. As an example of an identified magnetospheric compression event, Figure 2 shows the OMNI data and SYM/H index during 00–24 UT on 7 June 2014, where the two EMIC wave events, during 17:48–18:02 UT and 19:15–20:05UT, are closely associated with the fast growth of magnetospheric compression.

To identify those EMIC wave events that are closely associated with the fast growth of magnetospheric compression and also categorize them according to the SW drivers, the above two criteria are additionally applied to the EMIC wave events categorized in Table 1. The results of our additional identification are summarized in Table 2. Among the 210 EMIC wave events categorized in Table 1, we identified only 25 EMIC wave events as closely associated with the fast growth of magnetospheric compression. This gives us only a small fraction ∼12% of all EMIC wave events analyzed in this study (see the total occurrence rate in Table 2). Despite a small fraction, however, all the EMIC wave events identified in Table 2 are likely to be truly driven by the fast growth of magnetospheric compression. An overwhelming majority of EMIC wave events in Table 2 is observed during CME conditions in the upstream SW (∼76%), and only ∼24% of the compression-associated EMIC wave events are observed during HSS conditions. As one may expect, there are no EMIC wave events

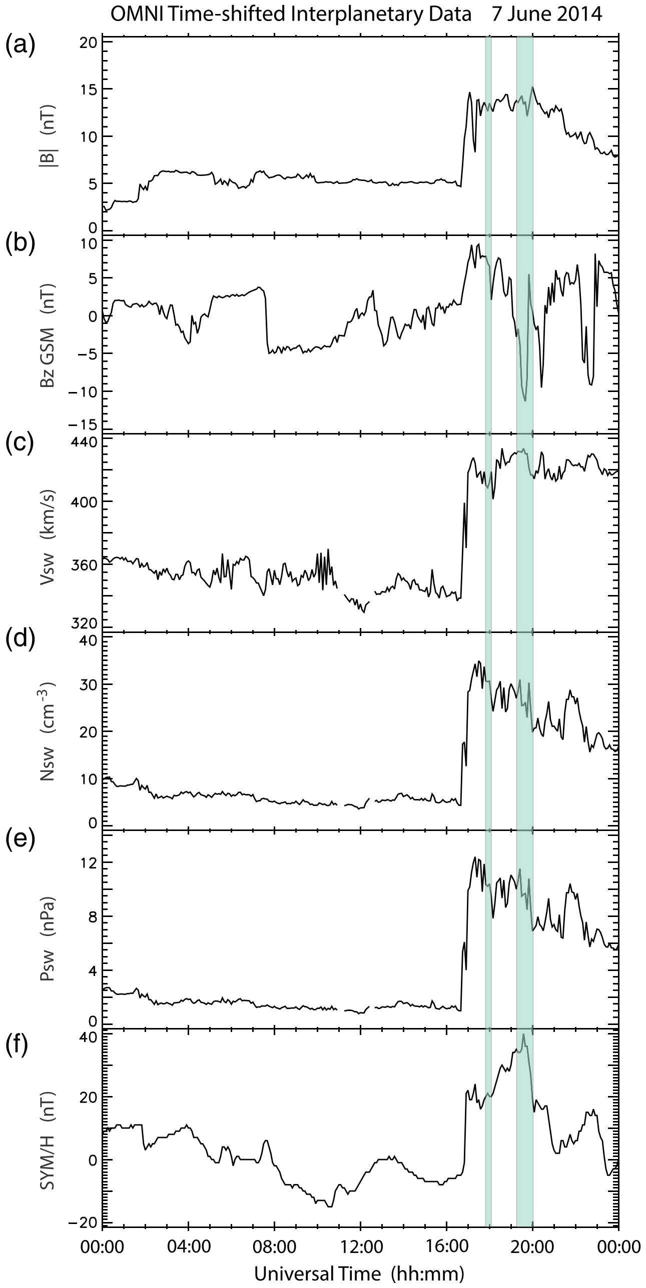

Figure 2. Magnetospheric compression as illustrated by 5-min time resolution OMNI data (panels a–e) and SYM/H index (panel f) during 00–24 UT on 7 June 2014. Panels (a) and (b) show the magnitude and north-south component of the IMF ($|B|$ and B_z, respectively), panel (c) shows the SW speed (V_{sw}), panel (d) shows the SW proton density (N_{sw}), and panel (e) shows the SW dynamic pressure (P_{sw}), all propagated in time to the nose of the Earth's bow shock. The two time intervals during which the EMIC wave events were observed are 17:48–18:02 UT (Probe A) and 19:15–20:05 UT (Probe B), and they are indicated by the shaded vertical bars.

closely associated with the fast growth of magnetospheric compression during QSW conditions. It is also important to emphasize that the ratio of CME events to HSS events in Table 2 (~3.2) is more than twice as high compared to that in Table 1 (~1.5). So the occurrence rate of EMIC wave events closely associated with the fast growth of magnetospheric compression is about twice as high during CME events than during HSS events. This fact is reflected by the occurrence rates in the bottom row of Table 2. This implies that instances of the fast growth of magnetospheric compression well above the quiet geomagnetic conditions are more frequent during CME conditions in the upstream SW than during HSSs. This also implies that the total

Table 2
Same as in Table 1, Except That Only EMIC Wave Events Closely Associated With the Fast Growth of Magnetospheric Compression Are Categorized

	CME in SW	HSS in SW	QSW	Total
Number of events	19	6	0	25
Percentage of events	76	24	0	100
Occurrence rate[a]	0.17	0.08	0	0.12

[a] Rate is calculated as a ratio of events here to the respective number in Table 1.

occurrence rate (~12%) found for the EMIC wave events closely associated with the fast growth of magnetospheric compression is likely to be even smaller for EMIC waves observed outside of the solar maximum during which the CME occurrence rates are greatest.

Table 3 shows the numbers of EMIC wave events closely associated with the fast growth of magnetospheric compression in four MLT bins. For each SW driver, the number of events in each MLT bin may be considered as an unnormalized event occurrence rate in that bin because (a) both Van Allen Probes completed an entire pass through all MLTs, that is, the probes' perigee-apogee lines precessed through all MLTs, during the analyzed period, (b) the spacecraft MLT-revolution speed does not depend on MLT, and (c) we may assume that all other observational parameters during the observed wave events are equally represented in all MLT bins. This means that for each SW driver in Table 3 the occurrence rate in each MLT bin can be obtained by multiplying the event number in that bin by a common normalization factor, which does not depend on MLT but only depends on the SW driver. For example, the occurrence rates here may be estimated with respect to the total number of EMIC wave events similar to those in Table 2. The results in Table 3 suggest that an occurrence rate of EMIC wave events closely associated with the fast growth of magnetospheric compression has a weak dependence on MLT, especially for the EMIC wave events during CME conditions. (Note that the number of events in different MLT bins is quite small, and so the statistics shown in Table 3 might not be representative and needs to be treated with care.) This differs qualitatively from the MLT distribution of the occurrence rate for EMIC waves driven by a permanent, slowly varying, QSW compression of the dayside magnetosphere that has a quite narrow maximum near noon (e.g., Park et al., 2016). Note that during the EMIC wave events closely associated with the fast growth of magnetospheric compression the distribution functions of energetic ions become unstable locally, and this process is likely to occur on a time scale smaller than both the ion gyro-period and bounce period. On the other hand, during QSW compression the modification of ion distributions takes place slowly, in the course of an adiabatic (both the first and second adiabatic invariants are conserved) ion drift from the nightside magnetosphere toward the dayside magnetosphere that leads to an EMIC wave generation near noon. Also, note that a detailed discussion of one EMIC wave event (a large event on 23 February 2014) included in Table 2 under the "CME in SW" category may be found in the paper by Engebretson et al. (2015).

3.4. Statistics of EMIC Waves on the SYM/H Index During CME, HSS, and QSW

Both the Dst index and SYM/H index characterize the level of geomagnetic activity at low latitudes (e.g., Fares Saba et al., 1997; Wanliss & Showalter, 2006) and are traditionally used as a proxy for the intensity of the magnetospheric RC. As EMIC waves are usually observed for the time intervals ranging from a few minutes, the SYM/H index could be a more appropriate index in describing the RC intensity in relation to EMIC waves. Below we use the SYM/H index with a moderate 5-min resolution. To present statistics of EMIC

Table 3
Number of EMIC Wave Events Closely Associated With the Fast Growth of Magnetospheric Compression in Different MLT Bins

MLT bins (hr)	0–6	6–12	12–18	18–24
CME-driven events	4	6	5	4
HSS-driven events	2	0	1	3
Total number of events	6	6	6	7

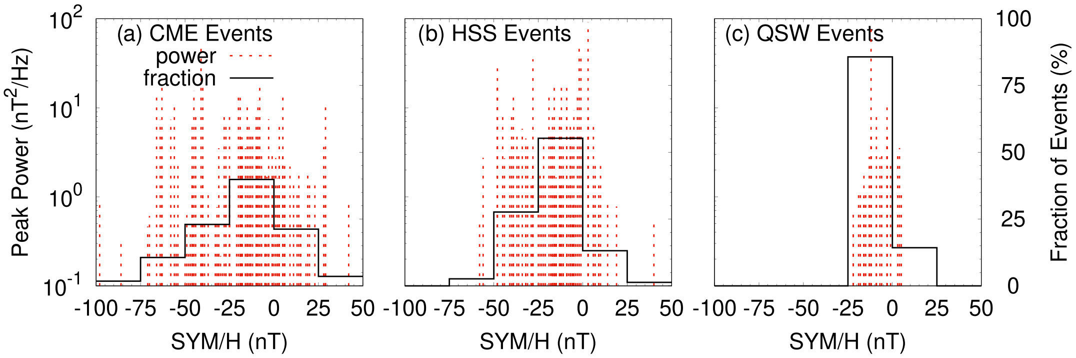

Figure 3. Peak power and fraction of the strongest EMIC wave events observed by the two Van Allen Probes from 1 October 2012 to 7 June 2014 as a function of the SYM/H index. Panels (a)–(c) show the statistics for EMIC waves observed during the CME, HSS, and QSW events, respectively. Note that fractions of events here should not be confused with the EMIC wave occurrence rates in different SYM/H bins.

waves as a function of the SYM/H index we show in Figure 3 the peak power and fraction of the strongest EMIC wave events observed by the two Van Allen Probes during 1 October 2012 through 7 June 2014 as a function of SYM/H. Figures 3a–3c show separately the statistics for EMIC waves observed during the CME, HSS, and QSW events, respectively. For each EMIC wave event, the shown SYM/H index is calculated as follows. If the event occurred fully within a 5-min window, we took the SYM/H index for that time window. If the event overlapped two or more 5-min windows, we took a weighted average of the respective SYM/H values. The fractions of EMIC wave events in Figure 3 are calculated in six SYM/H bins with the following boundaries: −100, −75, −50, −25, 0, 25, and 50 nT. For each SW driver, the calculated fractions give a ratio of EMIC wave events in a particular SYM/H bin to the respective total number of events from Table 1. The shown fractions should not be confused with the event occurrence rates in different SYM/H bins because the number of EMIC wave events in each bin depends not only on the event occurrence rate in this bin but also on the probability to observe a particular SYM/H bin during the given SW driver. The event fractions are shown here only to indicate the number of events in each bin.

Two features are immediately noticeable in Figure 3. (1) Very intense EMIC waves (with peak power >10 nT^2/Hz) are generated not only during CME and HSS conditions but also during QSW conditions as well. However, the number of very intense EMIC wave events during QSW conditions is small. (2) The SYM/H index during the CME-driven, HSS-driven, and QSW EMIC wave events is in the ranges of -100 nT $\lesssim$ SYM/H $\lesssim$ 40 nT, -60 nT $\lesssim$ SYM/H $\lesssim$ 40 nT, and -25 nT $\lesssim$ SYM/H $\lesssim$ 5 nT, respectively. The given SYM/H index ranges are obtained after analysis of EMIC wave events only and so do not necessary fully cover the typical SYM/H index ranges during CME, HSS, and QSW conditions. However, the given ranges qualitatively reflect the typical relative differences for the SYM/H indices observed during CME, HSS, and QSW conditions.

The third conclusion that can be drawn from Figures 3a and 3b is not that obvious and requires some additional analysis, which is given below. The fractions of EMIC wave events during magnetospheric compression elevated over the quiet geomagnetic compression, that is, during SYM/H >0, are ~25% and ~14% for the CME and HSS events, respectively (see Figures 3a and 3b). On the other hand, from Table 2 we can get the fractions 17% and 8% for EMIC wave events closely associated with the fast growth of magnetospheric compression during CME and HSS conditions, respectively. Then our third conclusion can be formulated as follows. (3) About two thirds (~68%) of the CME-induced EMIC wave events observed during the times of SYM/H >0 are actually the EMIC wave events closely associated with the fast growth of magnetospheric compression. For EMIC wave events during HSS, on the other hand, only about a half (~57%) of EMIC wave events observed during SYM/H >0 conditions are closely associated with the fast growth of magnetospheric compression. This implies that growth of magnetospheric compression during CME conditions more frequently takes a form of the fast and strong compression compared to that during HSS conditions.

Finally, let us comment on the QSW EMIC wave events in Figure 3c. As we already noticed in section 3.3, EMIC waves during QSW are observed even during quiet geomagnetic conditions when SYM/H ~ 0, and those waves are most easily generated around noon (e.g., Park et al., 2016). Of course, an increase of the

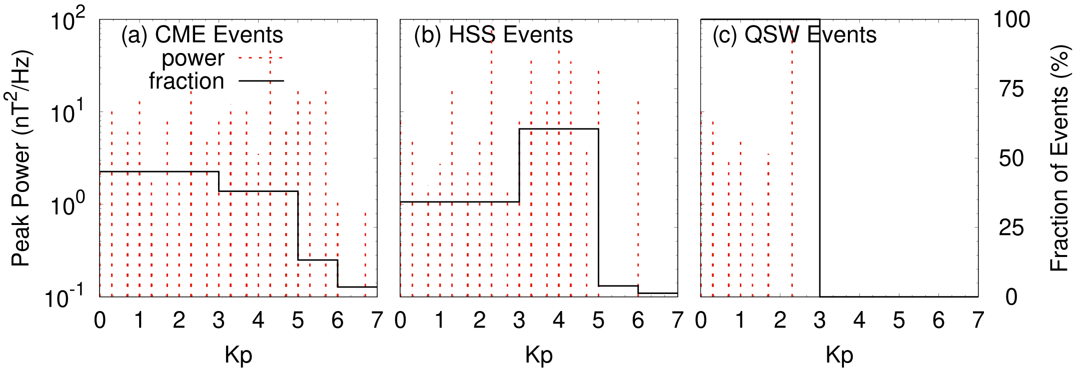

Figure 4. Same as in Figure 3, except as a function of Kp.

upstream SW dynamic pressure causes an additional compression of the dayside magnetosphere, so leading to the SYM/H index to become positive. There are three EMIC wave events in the region SYM/H >0 of Figure 3c (the largest SYM/H index there is 5 nT), and it is expected that an additional magnetospheric compression during those events should lead to an extension of the region around noon where EMIC waves are usually generated during QSW. However, in contrast to that expectation, all three EMIC wave events are observed at nightside MLTs (the event's MLTs are 3.9, 21, and 21.4 hr). So generation of the QSW EMIC wave events during the positive SYM/H index does not necessary take place around noon, and so is not solely related to an additional compression of the dayside magnetosphere. In section 3.7 we will provide a detailed discussion of the EMIC wave generation during QSW conditions.

3.5. Statistics of EMIC Waves on the Kp Index During CME, HSS, and QSW

The Kp index represents the level of geomagnetic activity at middle latitudes (e.g., Fares Saba et al., 1997) and is used as a proxy of strength of magnetospheric convection. We show in Figure 4 the peak power and fraction of the strongest EMIC wave events as a function of the 3-hr Kp index. Similar to Figure 3, Figures 4a–4c separately show the statistics for EMIC waves observed during CME, HSS, and QSW events, respectively. For each EMIC wave event, the shown Kp index is calculated as follows. If the event occurred fully within a 3-hr time frame of Kp, we took that value. If the event overlapped, we took a weighted average of the Kp values. The fractions of EMIC wave events in Figure 4 are calculated in four Kp bins with the following boundaries: 0, 3, 5, 6, and 7. Similar to Figure 3, the fractions in Figure 4 also should not be confused with the event occurrence rates in different Kp bins.

There are two major conclusions that can be drawn from Figure 4. (1) The Kp index during the CME-driven, HSS-driven, and QSW EMIC wave events is in the ranges of $0 \le \mathrm{Kp} \lesssim 6.7$, $0 \le \mathrm{Kp} \le 6$, and $0 \le \mathrm{Kp} \lesssim 2.3$, respectively. Similar to section 3.4, the above Kp ranges are also obtained after analysis of EMIC wave events only and so do not necessarily fully cover the typical Kp ranges during CME, HSS, and QSW conditions. However, the given ranges qualitatively reflect the typical relative differences for Kp indices during CME, HSS, and QSW conditions. (2) The fractions of the HSS-induced EMIC wave events have a strong maximum inside the Kp range of $\sim$3–5 (see Figure 4b), whereas the fractions of both the CME-induced and QSW EMIC wave events have maximum in the region of small Kp ($\mathrm{Kp} < 3$, see Figures 4a and 4c). This implies that strong magnetospheric convection takes place more frequently during HSS conditions than during both CME and QSW conditions. This is quite expected because the upstream SW speed is at the fast speed level during all the HSS events (see section 3.1.1). The electric field of magnetospheric convection, on the other hand, is proportional to the SW speed (e.g., Borovsky & Denton, 2006, and references therein), and so is the Kp index.

3.6. Statistics of EMIC Waves on the AE Index During CME, HSS, and QSW

The AE index is a measure of the strength of the auroral electrojet (e.g., Fares Saba et al., 1997) and is used as a proxy for the level of auroral and/or substorm activity. We show in Figure 5 the peak power and fraction of the strongest EMIC wave events as a function of the 5-min AE index. Similar to Figure 3, Figures 5a–5c separately show the statistics for EMIC waves observed during the CME, HSS, and QSW conditions, respectively. For each EMIC wave event, the shown AE index is calculated as follows. If the event occurred fully within a 5-min time frame of AE, we took that value. If the event overlapped, we took a weighted average of the respective AE values. The fractions of EMIC wave events in Figure 5 are calculated in four AE bins with

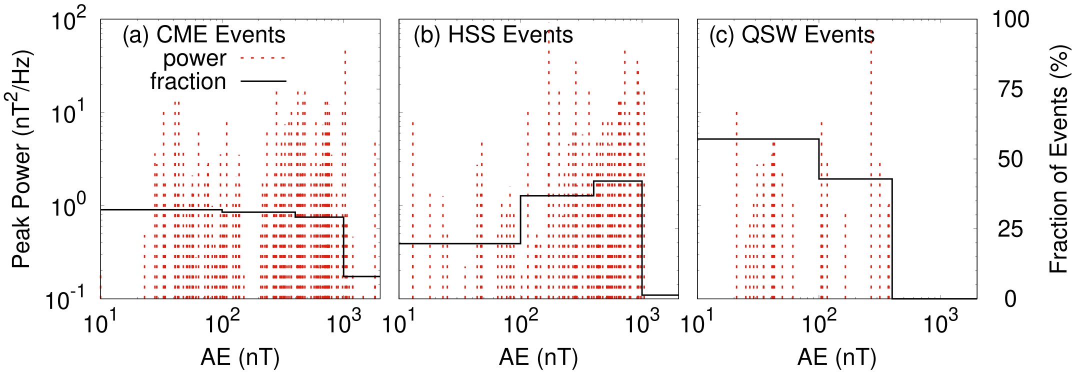

Figure 5. Same as in Figure 3, except as a function of AE.

the following boundaries: 10, 100, 400, 1,000, and 2,000 nT. Similar to Figure 3, the fractions in Figure 5 also should not be confused with the event occurrence rates in different AE bins.

There are two major conclusions that can be drawn from Figure 5. (1) The AE index during the CME-driven, HSS-driven, and QSW EMIC wave events is in the ranges of 10 nT $\lesssim$ AE $\lesssim$ 2,000 nT, 10 nT $\lesssim$ AE $\lesssim$ 1,000 nT, and 20 nT $\lesssim$ AE $\lesssim$ 400 nT, respectively. Similar to section 3.4, the above AE ranges are also obtained after analysis of EMIC wave events only and so do not necessary fully cover the typical AE ranges during CME, HSS, and QSW conditions. However, the given ranges qualitatively reflect the typical relative differences for the AE indices during CME, HSS, and QSW conditions. (2) The fractions of the HSS-induced EMIC wave events have a maximum inside the AE range of ~400–1,000 nT (see Figure 5b), whereas the fractions of the CME-induced EMIC wave events have a broad quasi-plateau inside the range of AE ~ 10–1,000 nT (see Figure 5a) that is followed by a steep decrease of fractions for AE > 1,000 nT, and the fractions of the QSW EMIC wave events have a maximum in the region of small AE (AE < 100 nT, see Figures 5c). These AE index dependencies are qualitatively similar to those shown above for the Kp index. So, as we noticed in section 3.5, a shift of the fraction maximum into the region of large AE indices for the HSS-induced EMIC wave event is due to stronger auroral activity, which itself is elevated due to the fact that the upstream SW speed is at the fast speed level during HSS conditions compared to that during CME and QSW conditions.

3.7. Statistics of EMIC Waves on MLT During CME, HSS, and QSW

To analyze statistics of EMIC wave events as a function of MLT we show in Figure 6 the peak power and fraction of the strongest EMIC wave events as a function of MLT. Similar to Figure 3, Figures 6a–6c separately show the statistics for EMIC waves observed during the CME, HSS, and QSW conditions, respectively. The fractions of EMIC wave events in Figure 6 are calculated in four MLT bins with the following boundaries: 0, 6, 12, 18, and 24 hr. It is important to stress here that in contrast to sections 3.4–3.6 the fractions of events shown in Figure 6 may be treated as unnormalized occurrence rates for EMIC waves in the different MLT bins (a justification for this is given in the comments on Table 3 in section 3.3). A most noticeable feature that

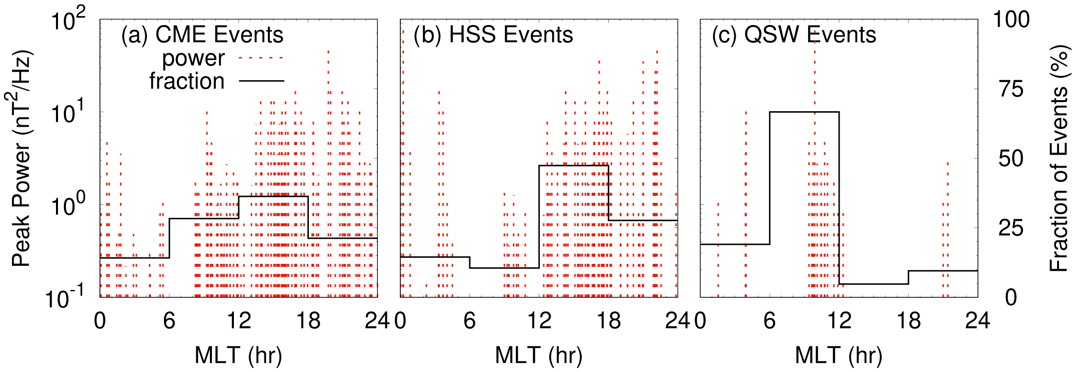

Figure 6. Same as in Figure 3, except as a function of MLT. In addition, in contrast to Figure 3, the fractions of events here may be considered as unnormalized occurrence rates for EMIC waves in the different MLT bins.

can be immediately observed in Figure 6 is the fact that the MLT distributions of EMIC wave fractions (or equally occurrence rates) for both the QSW and HSS events have a large dawn to dusk asymmetry, whereas the fractional distribution for the CME-induced EMIC waves is much more symmetric in the dawn to dusk direction. Below we analyze the underlying physics for the observed MLT distributions separately for the QSW, HSS-driven, and CME-driven EMIC wave events.

(1) For QSW conditions, a majority of EMIC wave events (~67%) is observed in the 6–12 hr MLT bin (mostly in the range of ~9–12 hr), while only ~19%, ~9%, and ~5% of events are observed in the 0–6, 18–24, and 12–18 hr MLT bins, respectively (see Figure 6c). So a majority of EMIC wave events (~86%) during QSW conditions is observed in the 0–12 hr MLT sector, whereas only ~14% of events are observed in the 12–24 hr MLT sector. The dawn to dusk asymmetry for the QSW EMIC wave events may be estimated as $\mathrm{ASY}_{6-18,\mathrm{QSW}} = F_{0-12}/F_{12-24} - 1 = 86/14 - 1 \sim 5.1$, where F_{0-12} and F_{12-24} are the fractions of EMIC wave events in the 0–12 and 12–24 hr MLT bins, respectively. Note that the number of QSW events is small (see Table 1), so the statistics for the QSW EMIC wave events might not be representative and needs to be treated thoughtfully. The results in Figure 6c agree well with the previously reported observations of a strong peak for an EMIC wave occurrence rate in the prenoon MLT hours during geomagnetically quiet conditions (e.g., Park et al., 2016; Saikin et al., 2016; Usanova et al., 2012). The results shown in Figure 6c can be qualitatively understood by considering the evolution of the RC ion temperature anisotropy $A = T_\perp/T_{||} - 1$, where $T_\perp$ and $T_{||}$ are the ion temperatures in the perpendicular and parallel to magnetic field directions, respectively. The RC ion temperature anisotropy usually provides a source of free energy for the EMIC wave generation in the Earth's inner magnetosphere if $A > A_{\mathrm{th}}$, where A_{th} is the positive threshold that depends on EMIC wave frequency and gyrofrequency of the unstable ions (e.g., Kennel & Petschek, 1996). (Note that positive temperature anisotropy is only a necessary, but not sufficient, condition for generation of EMIC waves.) Considering an energy anisotropy, which is proportional to the temperature anisotropy, instead of A, the above necessary condition for generation of EMIC waves takes the following form:

$$A_W = \frac{\langle W_\perp \rangle}{\langle W_{||} \rangle} > 2\left(1 + A_{\mathrm{th}}\right), \tag{1}$$

where A_W is the ion energy anisotropy and $\langle W_\perp \rangle$ and $\langle W_{||} \rangle$ are the ion average energies in the perpendicular and parallel to magnetic field directions, respectively. Both the large-scale convection electric field and substorm-associated inductive electric field are weak during QSW conditions (see Figures 4c and 5c). As a consequence, the inward energetic ion convection is also weak in the nightside magnetosphere. This weak inward convection usually cannot produce a level of temperature anisotropy that is high enough for local EMIC wave generation in the nightside magnetosphere before the gradient-curvature drift moves the energetic ions in the westward direction. As a result, the occurrence rate is small in the 18-24 hr MLT bin in Figure 6c. The injected energetic ions, however, continue to drift westward due to their gradient-curvature drift, as indicated by the negative SYM/H index in Figure 3c, toward the dayside magnetosphere. Because both the first and second adiabatic invariants are conserved during the ion drift, a change of the ion equatorial energies in the perpendicular and parallel to magnetic field directions between any two points (we mark them as "night" and "day") on the ion drift trajectory can be described by the following equation: (e.g., Baumjohann & Treumann, 1997)

$$\frac{W_{\perp,\mathrm{day}}}{\langle W_{||,\mathrm{day}} \rangle} \Bigg/ \frac{W_{\perp,\mathrm{night}}}{\langle W_{||,\mathrm{night}} \rangle} = \frac{B_{\mathrm{day}}}{B_{\mathrm{night}}} \frac{l_{\mathrm{day}}^2}{l_{\mathrm{night}}^2} \tag{2}$$

where $W_{\perp,\mathrm{day}}$ and $W_{\perp,\mathrm{night}}$ are the equatorial energy of a given ion in the perpendicular to magnetic field direction at the "day" and "night" points, respectively, B_{day} and B_{night} are the equatorial magnetic field at the "day" and "night" points, respectively, and l_{day} and l_{night} are the length of magnetic field line between the two mirror points for a given ion at the "day" and "night" point locations, respectively. Due to the permanent compression of the dayside magnetosphere, the general inequalities $B_{\mathrm{day}} > B_{\mathrm{night}}$ and $l_{\mathrm{day}} > l_{\mathrm{night}}$ hold along the drift trajectory of each ion (e.g., Roederer, 1970). (Note that $B_{\mathrm{day}} = B_{\mathrm{night}}$ for particles drifting with an equatorial pitch angle 90° if the electric field of magnetospheric convection, and so the $E \times B$ drift, is negligible.) So, as follows from Equation 2, the ratio of the perpendicular energy to the parallel energy grows for each ion during its drift from the nightside to the dayside magnetosphere. This means that energy anisotropy also grows, that is, $A_{W,\mathrm{day}} > A_{W,\mathrm{night}}$. As a consequence, this leads to the development of a large enough anisotropy which can cause EMIC wave generation in the dayside magnetosphere, whereas the initial ion anisotropy in the nightside region of injection is small and cannot lead to EMIC wave generation there. A slight displacement of the peak of the EMIC wave occurrence rate into the prenoon MLT hours is likely due to an asymmetry of the ion drift trajectories with respect to the noon-midnight line caused by the electric field of magnetospheric convection. In the case of no convection electric field, the gradient-curvature drift alone determines the drift trajectories of energetic ions, and these trajectories are symmetric with respect to the noon-midnight line (e.g., Figure 25 in Roederer, 1970). The convection electric field introduces the separatrix between the two different types of ion trajectories. The first type is formed by the closed ion trajectories that encircle Earth and are located inside the separatrix, where the gradient-curvature drift prevails. The second type is formed by the open trajectories that are located outside of the separatrix, where the $E \times B$ drift dominates the gradient-curvature one. Despite the convection electric field being weak during QSW conditions, this field causes energetic ions on the open drift trajectories to ultimately drift away from Earth in the pre-noon MLT sector due to a prevalence of the $E \times B$ drift there. This leads to the further growth of a positive ion anisotropy during the later stage of an ion drift in the prenoon MLT sector because the length of magnetic field line between the two mirror points continues to grow there. Note, however, that the equatorial magnetic field starts to decrease at some point along the ion drift trajectory in the prenoon MLT sector, so the ion anisotropy may also start to decrease at some point there. The few EMIC wave events observed in the nightside magnetosphere (see Figure 6c) indicate that the ion energy anisotropy required for EMIC wave generation (see Equation 1) can occasionally develop in the nightside magnetosphere even during QSW convection and substorm injection. EMIC wave events in the 0–6 hr MLT bin are likely to be generated by the low-energy ($\lesssim 5$ keV) RC ions (e.g., Anderson et al., 1996) whose drift is dominated by the $E \times B$ drift toward dawn. The events in the 18–24 hr MLT bin, however, are generated by higher-energy ions, which are drifting toward dusk due to the gradient-curvature drift.

(2) For the HSS events, ~47% and ~28% of EMIC wave events are observed in the 12–18 and 18–24 hr MLT bins, respectively, while only ~14% and ~11% of events are observed in the 0–6 and 6–12 hr MLT bins, respectively (see Figure 6b). So, in contrast to the QSW events, the majority of EMIC wave events (~75%) during HSS conditions is observed in the 12–24 hr MLT bin, whereas only ~25% of events is observed in the 0–12 hr MLT sector. The dawn to dusk asymmetry for the HSS events is $\mathrm{ASY}_{6-18,\mathrm{HSS}} = 25/75 - 1 \sim -0.7$. Despite the fact that the distribution of the EMIC wave occurrence rate in Figure 6b qualitatively differs from the distribution in Figure 6c, all the physical mechanisms outlined above as the mechanisms responsible for the development of ion temperature anisotropy and EMIC wave generation during QSW conditions also work during HSS conditions. First, EMIC waves in the prenoon MLT hours are also observed in Figure 6b (see the 6–12 hr MLT bin), and the physical mechanism of temperature anisotropy formation and EMIC wave generation there is the same as in the prenoon MLT hours during QSW conditions. However, the SW dynamic pressure during HSS conditions is elevated compared to that during QSW because the SW speed in the upstream flow is at the fast speed level during all the HSS events (see section 3.1.1). This causes an additional compression of the dayside magnetosphere. In particular this leads to a further extension of the region of increased compression into the postnoon 12–18 hr MLT bin. As a consequence, this leads to a further extension of the region where the necessary condition for EMIC wave generation (see Equation 1) starts to hold during the energetic ion drift from the nightside to the dayside magnetosphere. This creates more favorable conditions for EMIC wave generation in the 12–18 hr MLT bin (see Figure 6b) compared to the conditions there during QSW. Second, both the large-scale convection electric field and substorm-associated inductive electric field are stronger during HSS conditions (see Figures 4b and 5b) compared to those during QSW. This produces a larger temperature anisotropy in the nightside magnetosphere during an inward energetic ion convection and/or substorm injection. So the nightside anisotropy can be high enough to cause local EMIC wave generation there. This fact is reflected in a large occurrence rate in the 18–24 hr MLT bin in Figure 6b. Note that the temperature anisotropy is relaxing during EMIC wave generation. This causes some ions in the 18–24 hr MLT sector to precipitate in the loss cone before they can reach the dusk sector during their drift. However, the ions that still remain to be geomagnetically trapped near dusk continue to drift toward the dayside magnetosphere. For those trapped ions, their anisotropy starts to grow again due to compression of the dayside magnetosphere. Because the anisotropy of ions freshly injected in the nightside magnetosphere is higher during HSS conditions than during QSW (see above), the anisotropy in the 12–18 hr MLT bin is also higher, making the generation of EMIC waves in this MLT sector easier during HSS conditions compared to the QSW conditions. Similar to Figure 6c, the EMIC wave events in the 0–6 hr MLT bin of Figure 6b are also

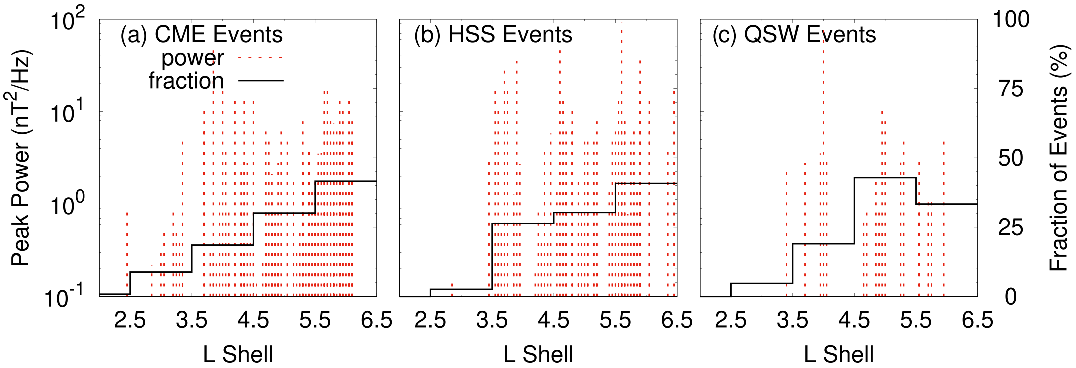

Figure 7. Same as in Figure 3, except as a function of L shell.

generated by the low-energy RC ions whose drift is dominated by the $E \times B$ drift toward dawn. Note, however, that energy of those "low-energy" ions is likely to be higher compared to the case of QSW conditions, because the convection electric field is much larger during the HSS events than during QSW.

(3) For the CME events, ~36%, ~29%, ~21%, and ~14% of EMIC wave events are observed in the 12–18, 6–12, 18–24, and 0–6 hr MLT bins, respectively (see Figure 6a). So ~57% of the EMIC wave events during CME are observed in the 12–24 hr MLT bin, and ~43% of events are observed in the 0–12 hr MLT bin. The dawn to dusk asymmetry for the CME events is $\mathrm{ASY}_{6-18,\mathrm{CME}} = 43/57 - 1 \sim -0.2$. Therefore, the dawn to dusk asymmetry during CME events is much smaller compared to that during both QSW and HSS events. All the physical mechanisms outlined above for HSS conditions as the mechanisms responsible for the development of temperature anisotropy and EMIC wave generation also work during CME conditions. However, a qualitative difference between Figures 6a and 6b is the fact that the relative occurrence rate for EMIC waves in the 6–12 hr MLT bin is substantially larger during CME conditions than that during HSS conditions. This may be due to a more disturbed magnetic field in the dayside magnetosphere during CME conditions compared to that during HSS. A more disturbed magnetic field is likely to be caused by an interplanetary shock, and/or a sheath of compressed SW, and/or ejecta, and/or a magnetic cloud during CME. Because the dayside ion anisotropy in Equation 2 depends on both the equatorial magnetic field and the length of the magnetic field line between the two mirror points there, a more disturbed magnetic field in the dayside magnetosphere may lead to an extension of the region of EMIC wave generation, that is, the region where Equation 1 holds, in the 6–12 hr MLT bin. Also note that the occurrence rate for the EMIC wave events closely associated with the fast growth of magnetospheric compression has a weak dependence on MLT during CME conditions (see Table 3), contributing to a more symmetric pattern of the MLT occurrence rate during CME conditions.

Finally, let us estimate the dayside to nightside asymmetries for the occurrence rates in Figure 6. These asymmetries can be estimated using the EMIC wave fractions given in the previous paragraphs of this section. For the QSW events, ~72% of EMIC wave events are observed in the dayside MLT = 6–18 hr sector, and ~28% of events are observed in the nightside MLT = 18–6 hr sector. So the dayside to nightside asymmetry may be estimated as $\mathrm{ASY}_{12-24,\mathrm{QSW}} = F_{6-18}/F_{18-6} - 1 = 72/28 - 1 \sim 1.6$, where F_{6-18} and F_{18-6} are the fractions

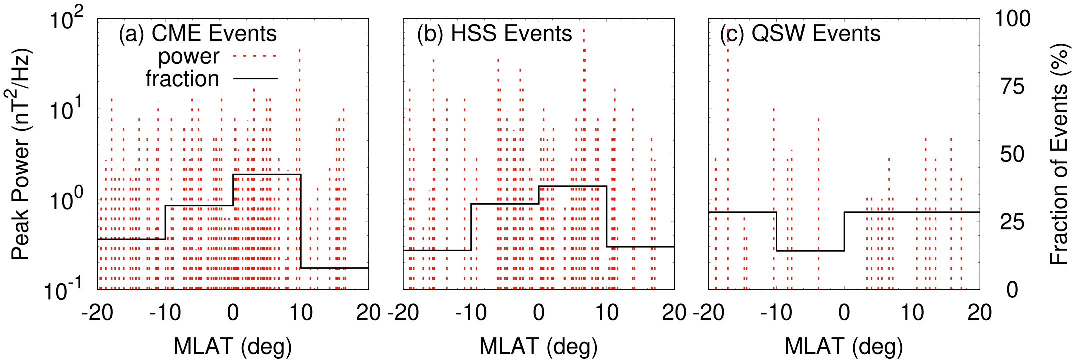

Figure 8. Same as in Figure 3, except as a function of MLAT.

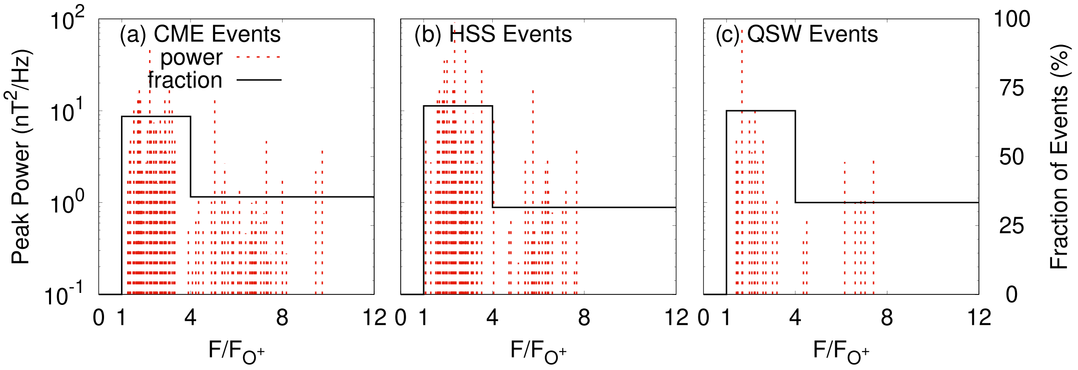

Figure 9. Same as in Figure 3, except as a function of wave frequency normalized by the local O^+ gyrofrequency. In addition, in contrast to Figure 3, the fractions of events here may be considered as unnormalized occurrence rates for EMIC waves in the different bins of normalized frequency.

of EMIC wave events in the 6–18 and 18–6 hr MLT bins, respectively. For the HSS events, ~58% of EMIC wave events are observed in the dayside MLT = 6–18 hr sector, and ~42% of events are observed in the nightside MLT = 18–6 hr sector. The dayside to nightside asymmetry for the HSS-induced EMIC wave events is $\mathrm{ASY}_{12-24,\mathrm{HSS}} = 58/42 - 1 \sim 0.4$. For the CME events, ~65% of EMIC wave events are observed in the dayside MLT = 6–18 hr sector, and ~35% of events are observed in the nightside MLT = 18–6 hr sector. So the dayside to nightside asymmetry during CME is $\mathrm{ASY}_{12-24,\mathrm{CME}} = 65/35 - 1 \sim 0.9$. Now we can formulate our fourth conclusion as follows. (4) A majority of EMIC wave events is observed in the dayside MLT sector independent of the SW driver. The largest dayside to nightside asymmetry for occurrence rates is observed for the QSW events being ~1.6, whereas the smallest asymmetry of ~0.4 takes place for the HSS-driven EMIC wave events. An intermediate dayside to nightside asymmetry of ~0.9 is observed for the CME-driven EMIC waves.

3.8. Statistics of EMIC Waves on L Shell During CME, HSS, and QSW

To analyze statistics of EMIC wave events as a function of L shell we show in Figure 7 the peak power and fraction of the strongest EMIC wave events as a function of L. Similar to Figure 3, Figures 7a–7c separately show the statistics for EMIC waves observed during CME, HSS, and QSW conditions, respectively. The fractions of EMIC wave events in Figure 7 are calculated in five L bins with the following boundaries: 2, 2.5, 3.5, 4.5, 5.5, and 6.5. Similar to Figure 3, the fractions in Figure 7 should not be confused with the event occurrence rates in different L bins, because they are not corrected for the probes' dwell time in different L bins that depends on L. Therefore, the event fractions are shown here only to indicate the number of events in each L bin. A major feature in Figure 7 can be formulated as follows. (1) The CME-driven, HSS-driven, and QSW EMIC wave events are distributed in the following L-ranges $2.5 \lesssim L \lesssim 6$, $3.5 \lesssim L \lesssim 6.5$, and $3.5 \lesssim L \lesssim 6$, respectively. So a majority of EMIC wave events observed by the two Van Allen Probes in the low L region below $L \sim 3.5$ (e.g., Gamayunov et al., 2018, and references therein) is observed during CME conditions in the upstream SW.

3.9. Statistics of EMIC Waves on MLAT During CME, HSS, and QSW

To analyze statistics of EMIC wave events on MLAT we show in Figure 8 the peak power and fraction of the strongest EMIC wave events as a function of MLAT. Similar to Figure 3, Figures 8a–8c separately show the statistics for EMIC waves observed during CME, HSS, and QSW conditions, respectively. The fractions of EMIC wave events in Figure 8 are calculated in four MLAT bins with the following boundaries: −20°, −10°, 0°, 10°, and 20°. Similar to Figure 3, the fractions in Figure 8 should not be confused with the event occurrence rates in different MLAT bins. This is true at least because a north to south asymmetry for the fraction of events in the near equatorial region of Figure 8 is likely to be unphysical but instead reflects a north to south asymmetry in the Van Allen Probes sampling due to the probes' orbits. Two major conclusions from Figure 8 can be formulated as follows. (1) Independent of the SW driver, EMIC waves are observed in the entire MLAT range accessible to the Van Allen Probes. (2) For both the CME and HSS events, the fractions of events have a strong maximum in the near equatorial region of $|\mathrm{MLAT}| \lesssim 10°$, where ~73% and ~70% of the CME-induced and HSS-induced EMIC wave events are, respectively, observed. The distribution of fractions for the QSW EMIC wave events, on the other hand, has a weak minimum in the near equatorial

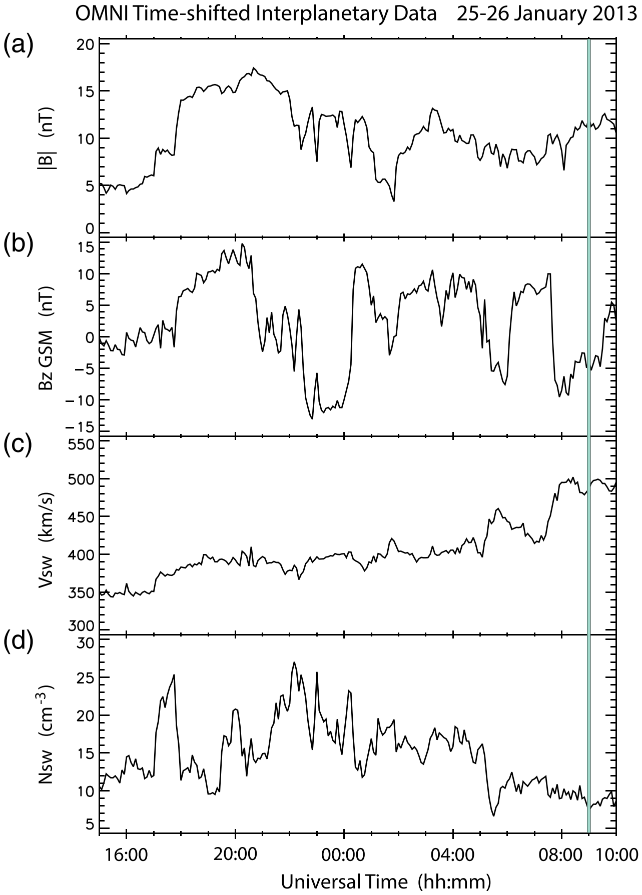

Figure A1. Growth phase of an HSS event as illustrated by the 5-min time resolution OMNI data from 15 UT on 25 January to 10 UT on 26 January 2013. Panels (a) and (b) show the magnitude and north-south component of the IMF ($|B|$ and B_z, respectively), panel (c) shows the SW speed ($V_{\rm sw}$), and panel (d) shows the SW proton density ($N_{\rm sw}$), all propagated in time to the nose of the Earth's bow shock. The time interval during which the EMIC wave event was observed by Probe A is 08:58–09:02 UT, and it is indicated by the shaded vertical bar.

region of $|\mathrm{MLAT}| \lesssim 10°$, where $\sim$43% of EMIC wave events are observed. (As we noted above, the number of the QSW EMIC wave events is small, and so the above conclusion regarding a minimum of the QSW EMIC wave events in the near equatorial region might be considered as a likely one.)

3.10. Statistics of EMIC Waves on Frequency During CME, HSS, and QSW

To analyze statistics of EMIC wave events as function of frequency we show in Figure 9 the peak power and fraction of the strongest EMIC wave events as a function of wave frequency normalized by the local O^+ gyrofrequency. Similar to Figure 3, Figures 9a–9c separately show the statistics for EMIC waves observed during CME, HSS, and QSW conditions, respectively. The fractions of EMIC wave events in Figure 9 are calculated in three bins for normalized frequency with the following boundaries: 0, 1, 4, and 16. Similar to the MLT fractions in section 3.7, the fractions shown in Figure 9 also may be treated as unnormalized occurrence rates for EMIC waves in the different bins of normalized frequency. Two major features observed in Figure 9 can be formulated as follows. (1) Independent of the SW driver, no strong EMIC wave events are observed in the frequency range of $F/F_{O+} \leq 1$, whereas $\sim$65–70% of EMIC wave events are observed in the range of $F/F_{O+} = 1$–4, and $\sim$30–35% of events are observed in the range $F/F_{O+} > 4$ (mostly below $F/F_{O+} \sim 8$). (2) There is no frequency stopband immediately above $F/F_O^+ = 4$ for the EMIC wave events observed during CME conditions (see Figure 9a), whereas for both the HSS-induced and QSW EMIC wave events the He^+ stopband is clearly seen, except one EMIC wave event in Figure 9b that has normalized frequency $F/F_{O+} \gtrsim 4$. Note that there is a possibility that the CME-driven EMIC waves with $F/F_{O+} \sim 4$ are generated in the near equatorial region with the frequencies above the equatorial He^+ stopband, but observed in the

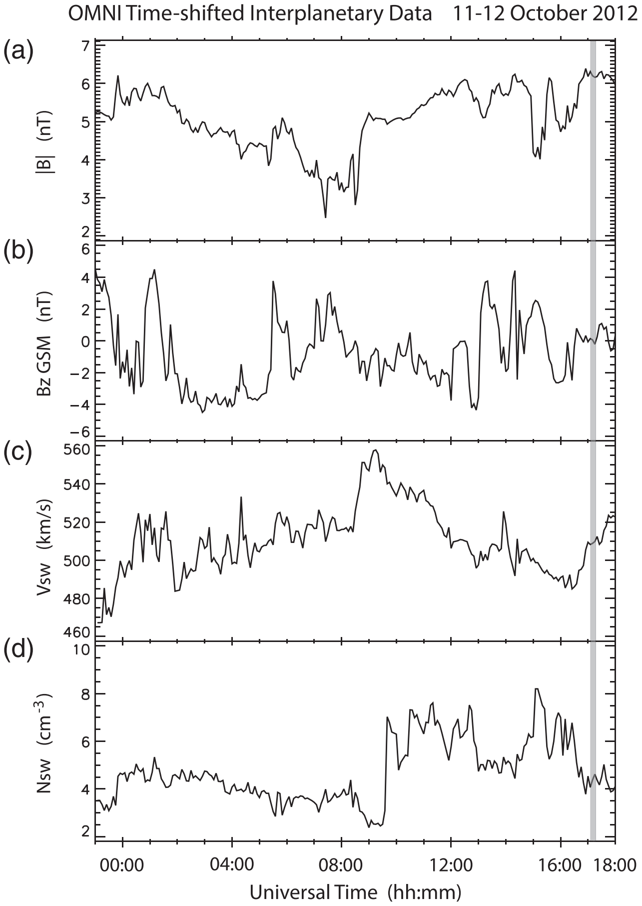

Figure A2. Quasi-plateau phase of an HSS event as illustrated by the 5-min time resolution OMNI data from 23 UT on 11 October to 18 UT on 12 October 2012. Panels (a)–(d) show the same parameters as in Figure A1, and the time interval during which the EMIC wave event was observed by Probe A is 17:08–17:15 UT.

off-equatorial region of generation, that is, in the region of larger magnetic field where their normalized frequencies become $\lesssim 4$. If this scenario takes place, then the majority of events with the normalized frequency ~4 should be observed in the off-equatorial region. To check the above possibility, we looked separately at the off-equatorial CME-driven EMIC wave events observed in the region of |MLAT| >10°. Among 30 EMIC wave events in this off-equatorial region, 21 events (70%) and 7 events (23%) have normalized frequencies $F/F_{O^+} < 2.7$ and $F/F_{O^+} > 4.9$, respectively, that is, not close to 4. Only two events have normalized frequencies 3.9 and 4.4, that is, around 4. So the latter two events may be potentially generated in the near equatorial region. In Figure 9a, however, essentially more than two events have normalized frequencies $F/F_{O^+} \sim 4$. In addition, the percentages of the off-equatorial CME-driven EMIC wave events in the different frequency bands are quite close to those in the entire MLAT range, indicating that the effects of wave propagation and/or separation of the regions of wave generation and observation are small. So the results stated in the above Item (2) suggest that the fraction of He^+ in the background plasma may be negligible during CME conditions, while the contribution of thermal He^+ in the EMIC wave dispersion relation may be substantial during both HSS and QSW events. This suggestion does not contradict Item (1) formulated above, because the EMIC wave growth rates in the inner magnetosphere usually maximize in the frequency range of $F/F_{O^+} \sim 1$–4 independent of the heavy ion composition in background plasma (see, e.g., Figure 2 in Khazanov et al., 2003).

4. Summary

In this paper we have analyzed the statistics of EMIC waves observed in the Earth's inner magnetosphere during CME, HSS, and QSW conditions in the upstream SW. Such an analysis has been done here for the first time. For our analysis we have used the EMIC wave observations by the two Van Allen Probes during the

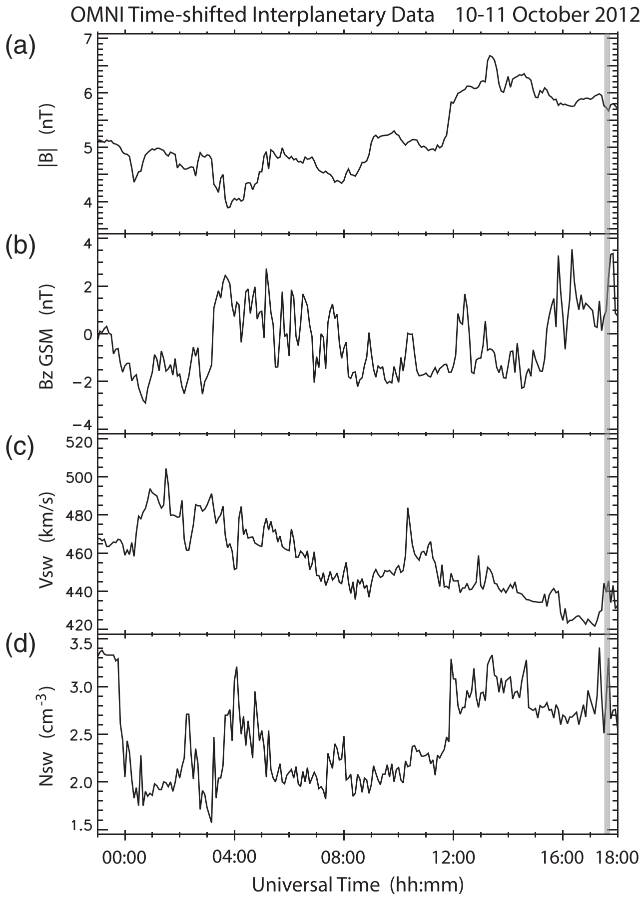

Figure A3. Declining phase of an HSS event as illustrated by the 5-min time resolution OMNI data from 23 UT on 10 October to 18 UT on 11 October 2012. Panels (a)–(d) show the same parameters as in Figure A1, and the time interval during which the EMIC wave event was observed by Probe A is 17:32–17:36 UT.

time period from 1 October 2012 to 7 June 2014 (during the first MLT revolution of Van Allen Probes), when the solar maximum of the 24th solar cycle has taken place. Among all EMIC wave events observed by the two probes, only the strongest events with peak wave power greater than 10^{-1} nT^2/Hz have been considered here. This totals to 211 strongest EMIC wave events observed by the two Van Allen Probes during their first MLT revolution. The major results and conclusions of our analysis can be summarized as follows.

(1) Quantitative criteria to identify the CME, HSS, and QSW events in the upstream SW data are formulated. These criteria can be routinely used in any future works where an automatic identification of the CME, HSS, and QSW events in upstream SW data is needed.
(2) A majority of EMIC wave events (~54%) is observed during CME conditions, whereas ~36% and ~10% of events are observed during HSS and QSW, respectively.
(3) Out of 211 EMIC wave events analyzed here, only 25 events are identified as closely associated with the fast growth of magnetospheric compression. This is ~12% of all EMIC wave events analyzed in this study. Among 25 EMIC wave events closely associated with the fast growth of magnetospheric compression, ~76% are observed during CME conditions, whereas ~24% and 0% of events are observed during HSS and QSW conditions, respectively. The occurrence rate for EMIC wave events closely associated with the fast growth of magnetospheric compression has a weak dependence on MLT, especially for the CME-driven EMIC wave events.
(4) The CME-driven EMIC wave events are observed within the following limits of SYM/H, Kp, and AE indices: -100 nT $\lesssim$ SYM/H $\lesssim$ 40 nT, 0 $\leq$ Kp $\lesssim$ 6.7, and 10 nT $\lesssim$ AE $\lesssim$ 2000 nT. The HSS-driven EMIC wave events are observed within the following limits of SYM/H, Kp, and AE indices: −60 nT $\lesssim$ SYM/H $\lesssim$ 40 nT, 0 $\leq$ Kp $\leq$ 6, and 10 nT $\lesssim$ AE $\lesssim$ 1,000 nT. The QSW EMIC wave events are observed within the following limits of SYM/H, Kp, and AE indices: −25 nT $\lesssim$ SYM/H $\lesssim$ 5 nT, 0 $\leq$ Kp $\lesssim$ 2.3, and

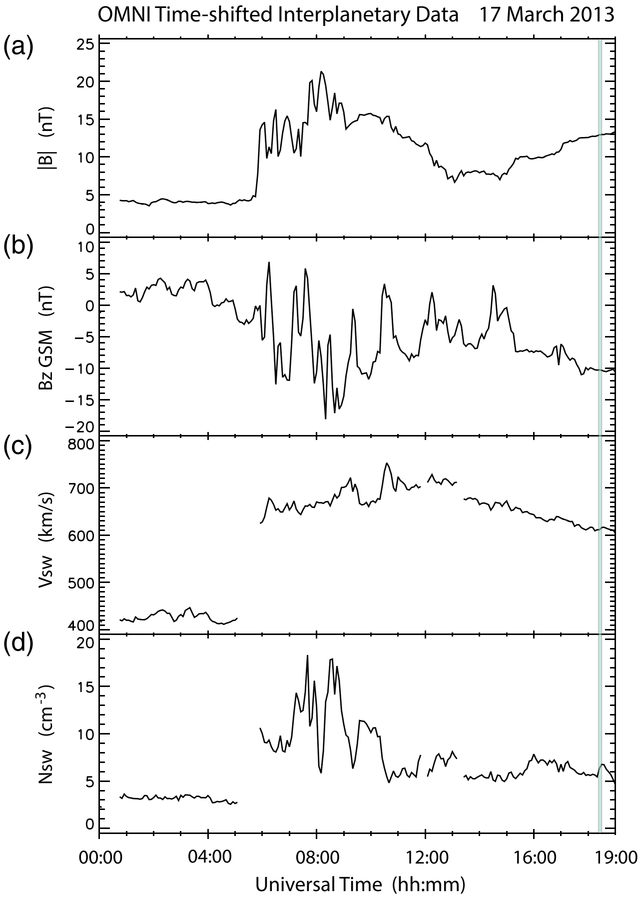

Figure A4. Shock phase of a CME event as illustrated by the 5-min time resolution OMNI data during 00–19 UT on 17 March 2013. Panels (a)–(d) show the same parameters as in Figure A1, and the time interval during which the EMIC wave event was observed by Probe A is 18:24– 18:28 UT.

20 nT $\lesssim$ SYM/H $\lesssim$ 400 nT. Although the given index ranges are obtained after analysis of EMIC wave events only and so do not necessary fully cover the typical index ranges during CME, HSS, and QSW conditions, the given ranges qualitatively reflect the typical relative differences for the above indices during CME, HSS, and QSW conditions.

(5) A majority of the QSW EMIC wave events (~72%) is observed in the ~9–12 hr MLT sector, and maximum of the wave occurrence rate is also located in this sector. A majority of the HSS-induced EMIC wave events (~75%) is observed in the ~12–24 hr MLT sector with the maximum of wave occurrence rate in the 12–18 hr MLT bin. A majority of the CME-induced EMIC wave events (~86%) is observed in the ~8–24 hr MLT sector with the maximum of wave occurrence rate in the 12–18 hr MLT-bin.

(6) The CME-driven, HSS-driven, and QSW EMIC wave events are observed in the following L ranges: $2.5 \lesssim L \lesssim 6$, $3.5 \lesssim L \lesssim 6.5$, and $3.5 \lesssim L \lesssim 6$, respectively. So a majority of EMIC wave events observed by Van Allen Probes in the low L region is observed during CME conditions in the upstream SW.

(7) Independent of the SW driver, EMIC wave events are observed in the entire MLAT range accessible to the Van Allen Probes. The fractions of EMIC wave events during both the CME and HSS conditions have a strong maximum in the near equatorial region of $|\mathrm{MLAT}| \lesssim 10°$. On the other hand, distribution of fractions for the QSW EMIC wave events is likely to have a minimum in the near equatorial region.

(8) Independent of the SW driver, no strong EMIC wave events are observed in the frequency range below the local O^+ gyrofrequency, whereas ~65–70% of events are observed in the range $F/F_{O^+} = 1$–4, and ~30–35% of events are observed in the frequency range above the local He^+ gyrofrequency, that is, for $F/F_{O^+} > 4$. The absence of a distinct frequency stopband immediately above $F/F_{O^+} = 4$ for the EMIC wave events observed during CME conditions suggests that the fraction of He^+ in the background

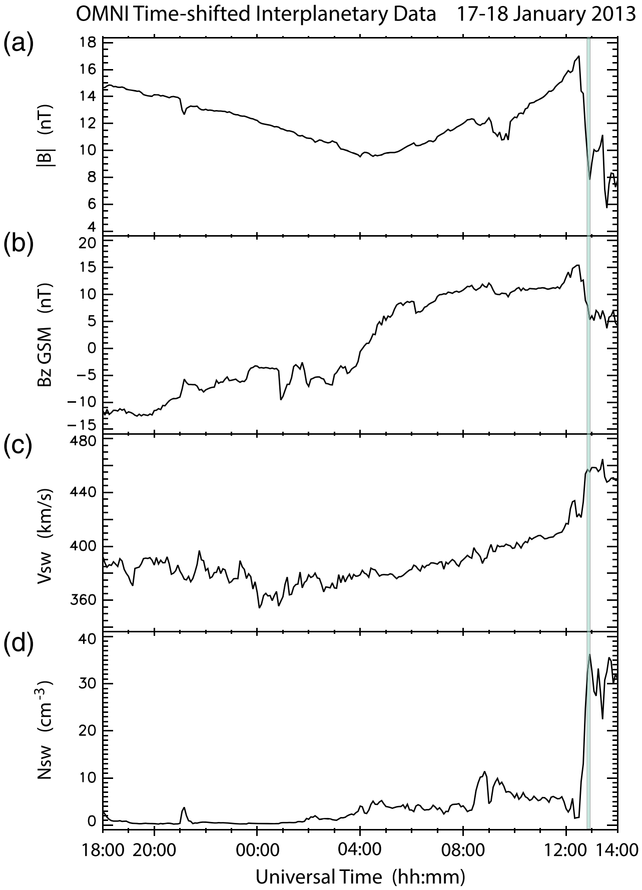

Figure A5. Magnetic cloud phase of a CME event as illustrated by the 5-min time resolution OMNI data from 18 UT on 17 January to 14 UT on 18 January 2013. Panels (a)–(d) show the same parameters as in Figure A1, and the time interval during which the EMIC wave event was observed by Probe A is 12:50–12:55 UT.

plasma may be negligible during CME conditions, while a contribution of thermal He$^+$ in an EMIC wave dispersion relation may be essential during both HSS and QSW conditions.

As we noted above, this paper is the first one where the EMIC wave statistics are analyzed with respect to the upstream SW drivers. For this reason, a large amount of our effort has been devoted to the development and formulation of quantitative criteria to routinely identify the CME, HSS, and QSW conditions in the upstream SW. For the same reason, we have presented here only the general context of EMIC waves observed during CME, HSS, and QSW conditions, touching only the most common characteristics of plasma and EMIC waves observed during the analyzed SW drivers. We have not analyzed here the detailed microphysics of the EMIC wave generation as was done before, for example, by Gamayunov et al. (2018). Such a detailed analysis of EMIC wave generation should be done in the future, because the physics of EMIC wave generation is different in the different spatial regions of the magnetosphere (e.g., Gamayunov et al., 2018), and likely during different SW drivers. Finally, we would like to explicitly emphasize that a further analysis of EMIC wave properties as a function of the CME, HSS, and QSW driving conditions in the upstream SW is needed during the entire solar cycle as well to fully understand and explain observations of EMIC waves in the Earth's magnetosphere.

Appendix A: IMF and SW Data During the Distinctive Phases of HSS, CME, and QSW Events

Figure A1 shows the OMNI data during the growth phase of the HSS event observed before and during the EMIC wave event observed by Van Allen Probe-B during 08:58–09:02 UT on 26 January 2013. In this figure, V_{sw} grows from the slow SW level, and $V_{sw} \gtrsim 400$ km/s starting from ~20 UT on 25 January. The

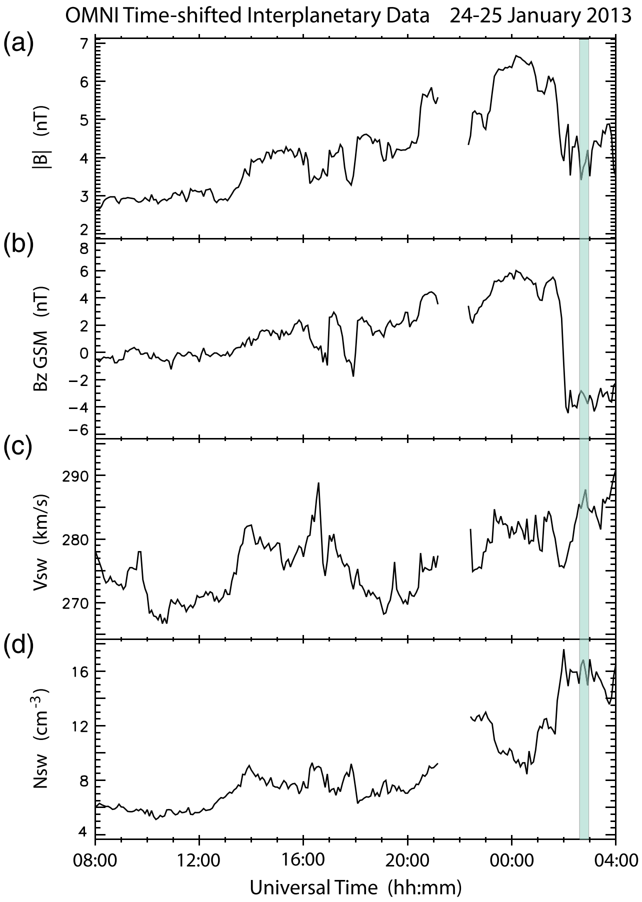

Figure A6. Ejecta phase of a CME event as illustrated by the 5-min time resolution OMNI data from 08 UT on 24 January to 04 UT on 25 January 2013. Panels (a)–(d) show the same parameters as in Figure A1, and the time interval during which the EMIC wave event was observed by Probe B is 02:35–02:55 UT.

SW acceleration is accompanied by peaks of $N_{\rm sw} > 10\,{\rm cm}^{-3}$ and $|B| > 10$ nT, and also by the oscillations of B_z with $|B_z| \gtrsim 10$ nT. So all the conditions specified in Item 1 of section 3.1.1 are met.

Figure A2 shows the OMNI data during the quasi-plateau phase of the HSS event observed before and during the EMIC wave event observed by Van Allen Probe-A during 17:08–17:15 UT on 12 October 2012. In this figure, $V_{\rm sw}$ has a quasi-plateau at the fast SW level of $\gtrsim 500$ km/s, and it fluctuates with $\gtrsim 20$ km/s peak-to-peak. B_z also fluctuates with $\gtrsim 3$ nT peak-to-peak. So all the conditions specified in Item 2 of section 3.1.1 are met.

Figure A3 shows the OMNI data during the declining phase of the HSS event observed before and during the EMIC wave event observed by Van Allen Probe-A during 17:32–17:36 UT on 11 October 2012. In this figure, $V_{\rm sw}$ decreases from the fast SW level of ~500 km/s to the slow SW level starting from ~1 UT on 11 October. The SW deceleration is accompanied by fluctuations of both $V_{\rm sw}$ and B_z with peak-to-peak amplitudes of $\gtrsim$ 20 km/s and $\gtrsim$ 3 nT, respectively. So all the conditions specified in Item 3 of section 3.1.1 are met.

Figure A4 shows the OMNI data during the shock phase of the CME event observed before and during the EMIC wave event observed by Van Allen Probe-A during 18:24–18:28 UT on 17 March 2013. In this figure, a shock-like jump in $V_{\rm sw}$, $N_{\rm sw}$, and $|B|$ is observed just before 06 UT. So all the conditions specified in Item 1 of section 3.1.2 are met.

Figure A5 shows the OMNI data during the magnetic cloud phase of the CME event observed before the EMIC wave event observed by Van Allen Probe-A during 12:50–12:55 UT on 18 January 2013. In this figure, $|B| \gtrsim 10$ nT all the time before the EMIC wave event, and it slowly changes with time. A smooth change of

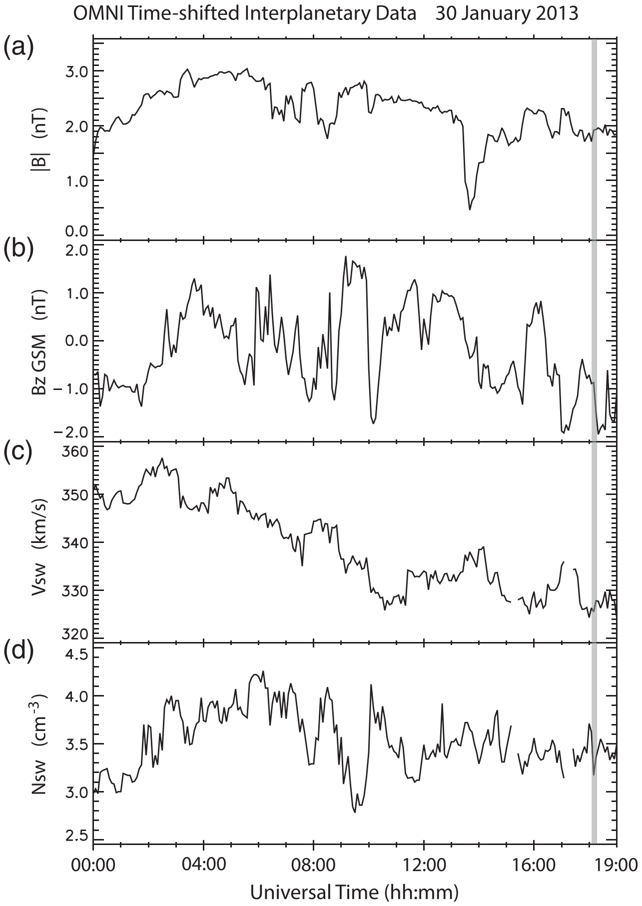

Figure A7. A QSW event as illustrated by the 5-min time resolution OMNI data during 00-19 UT on 30 January 2013. Panels (a)–(d) show the same parameters as in Figure A1, and the time interval during which the EMIC wave event was observed by Probe B is 18:10–18:15 UT.

B_z is also observed, indicating rotation of the IMF. So the conditions specified in Item 2 of section 3.1.2 are met. Note that during the EMIC wave event itself the ejecta trailing the magnetic cloud appear.

Figure A6 shows the OMNI data during the ejecta phase of the CME event observed before and during the EMIC wave event observed by Van Allen Probe-B during 02:35–02:55 UT on 25 January 2013. In this figure, a smooth growth of N_{sw} from ~6 cm^{-3} up to ~18 cm^{-3} is observed. So the conditions specified in Item 3 of section 3.1.2 are met.

Figure A7 shows the OMNI data during the QSW event observed before and during the EMIC wave event observed by Van Allen Probe-B during 18:10–18:15 UT on 30 January 2013. In this figure, V_{sw} is at the slow SW level of <360 km/s during 100% of time. In addition, Items 1–3 from section 3.1.2 are not satisfied. So the conditions specified in Item 1 of section 3.1.3 are met.

Data Availability Statement

The sunspot number data used here are available at SILSO, Royal Observatory of Belgium, Brussels (http://www.sidc.be/silso/datafiles). CDF files of Van Allen Probes EMFISIS data are available at this site (http://emfisis.physics.uiowa.edu). SW and IMF data as well as SYM/H index data are available at the Goddard Space Flight Center Space Physics Data Facility (https://cdaweb.sci.gsfc.nasa.gov/index.html/). Dst, Kp, and AE data are available at this site (http://cdaweb.gsfc.nasa.gov) via the `OMNI2_H0_MRG1HR` and `OMNI_HRO_1MIN` databases. The data set of the 211 strongest EMIC wave events analyzed here is available at these sites (https://scholar.colorado.edu/concern/datasets/vq27zp38c and/or https://doi.org/10.25810/fze6-7391).

Acknowledgments

This paper is based on work supported by the National Aeronautics and Space Administration (NASA) under Grant 80NSSC18K1221.

References

Anderson, B. J., Denton, R. E., Ho, G., Hamilton, D. C., Fuselier, S. A., & Strangeway, R. J. (1996). Observational test of local proton cyclotron instability in the Earth's magnetosphere. *Journal of Geophysical Research*, *101*(A10), 21,527–21,543.

Anderson, B. J., Erlandson, R. E., & Zanetti, L. J. (1992a). A statistical study of Pc 1-2 magnetic pulsations in the equatorial magnetosphere: 1. Equatorial occurrence distributions. *Journal of Geophysical Research*, *97*, 3075. https://doi.org/10.1029/91JA02706

Anderson, B. J., Erlandson, R. E., & Zanetti, L. J. (1992b). A statistical study of Pc 1-2 magnetic pulsations in the equatorial magnetosphere: 2. Wave properties. *Journal of Geophysical Research*, *97*, 3089. https://doi.org/10.1029/91JA02697

Anderson, B. J., & Fuselier, S. A. (1994). Response of thermal ions to electromagnetic ion cyclotron waves. *Journal of Geophysical Research*, *99*, 19413.

Baker, D. N., Pulkkinen, T. I., Li, X., Kanekal, S. G., Ogilvie, K. W., Lepping, R. P., et al. (1998). A strong CME-related magnetic cloud interaction with the Earth's magnetosphere: ISTP observations of rapid relativistic electron acceleration on May 15, 1997. *Geophysical Research Letters*, *25*, 2975.

Baumjohann, W., & Treumann, R. A. (1997). *Basic space plasma physics*. London: Imperial College Press.

Bingham, S. T., Mouikis, C. G., Kistler, L. M., Paulson, K. W., Farrugia, C. J., Huang, C. L., et al. (2019). The storm time development of source electrons and chorus wave activity during CME- and CIR-driven storms. *Journal of Geophysical Research: Space Physics*, *124*, 6438–6452. https://doi.org/10.1029/2019JA026689

Borovsky, J. E., & Denton, M. H. (2006). Differences between CME-driven storms and CIR-driven storms. *Journal of Geophysical Research*, *111*, A07S08. https://doi.org/10.1029/2005JA011447

Borovsky, J. E., Thomsen, M. F., & Elphic, R. C. (1998). The driving of the plasma sheet by the solar wind. *Journal of Geophysical Research*, *103*(A8), 17,617–17,639.

Burlaga, L. F., Lepping, R., & Jones, J. (1990). Global configuration of a magnetic cloud. In C. T. Russell, E. R. Priest, & L. C. Lee (Eds.), *Physics of flux ropes* (Vol. 58, pp. 373). Washington, DC: American Geophysical Union.

Burlaga, L. F., Klein, L., Sheeley, N. R., Bichels, D. J., Howard, R. A., Koomen, M. J., et al. (1982). A magnetic cloud and a coronal mass ejection. *Geophysical Research Letters*, *9*(12), 1317.

Claudepierre, S. G., Elkington, S. R., & Wiltberger, M. (2008). Solar wind driving of magnetospheric ULF waves: Pulsations driven by velocity shear at the magnetopause. *Journal of Geophysical Research*, *113*, A05218. https://doi.org/10.1029/2007JA012890

Claudepierre, S. G., Hudson, M. K., Lotko, W., Lyon, J. G., & Denton, R. E. (2010). Solar wind driving of magnetospheric ULF waves: Field line resonances driven by dynamic pressure fluctuations. *Journal of Geophysical Research*, *115*, A11202. https://doi.org/10.1029/2010JA015399

Claudepierre, S. G., Wiltberger, M., Elkington, S. R., & Hudson, M. K. (2009). Magnetospheric cavity modes driven by solar wind dynamic pressure fluctuations. *Geophysical Research Letters*, *36*, L13101. https://doi.org/10.1029/2009GL039045

Clausen, L. B. N., Baker, J. B. H., Ruohoniemi, J. M., & Singer, H. J. (2011). EMIC waves observed at geosynchronous orbit during solar minimum: Statistics and excitation. *Journal of Geophysical Research*, *116*, A10205. https://doi.org/10.1029/2011JA016823

Clemmons, J. H., Pfaff, R. F., Lennartsson, O. W., Mozer, F. S., Singer, H. J., Peterson, W. K., et al. (2000). Observations of traveling Pc5 waves and their relation to the magnetic cloud event of January 1997. *Journal of Geophysical Research*, *105*(A3), 5441.

Cornwall, J. M., Coroniti, F. V., & Thorne, R. M. (1971). Unified theory of SAR arc formation at the plasmapause. *Journal of Geophysical Research*, *76*, 4428.

Dungey, J. W. (1955). Electrodynamics of the outer atmosphere. In *Physics of the Ionosphere* (p. 229). London: Phys. Soc. London.

Dungey, J. W. (1961). Interplanetary magnetic field and the auroral zones. *Physical Review Letters*, *6*, 47.

Engebretson, M. J., Posch, J. L., Wygant, J. R., Kletzing, C. A., Lessard, M. R., Huang, C.-L., et al. (2015). Van Allen probes, NOAA, GOES, and ground observations of an intense EMIC wave event extending over 12 h in magnetic local time. *Journal of Geophysical Research: Space Physics*, *120*, 5465–5488. https://doi.org/10.1002/2015JA021227

Fares Saba, M. M., Gonzalez, W. D., & Clúa de Gonzalez, A. L. (1997). Relationships between the AE, AP and Dst indices near solar minimum (1974) and at solar maximum (1979). *Annales Geophysicae*, *15*, 1265–1270. https://doi.org/10.1007/s00585-997-1265-x

Fraser, B. J., Grew, R. S., Morley, S. K., Green, J. C., Singer, H. J., Loto'aniu, T. M., & Thomsen, M. F. (2010). Storm time observations of electromagnetic ion cyclotron waves at geosynchronous orbit: GOES results. *Journal of Geophysical Research*, *115*, A05208. https://doi.org/10.1029/2009JA014516

Fuselier, S. A., Petrinec, S. M., & Trattner, K. J. (2000). Stability of the high-latitude reconnection site for steady northward IMF. *Geophysical Research Letters*, *27*(4), 473. https://doi.org/10.1029/1999GL003706

Gamayunov, K. V., & Khazanov, G. V. (2007). Effect of oblique electromagnetic ion cyclotron waves on relativistic electron scattering: Combined Release and Radiation Effects Satellite (CRRES)-based calculation. *Journal of Geophysical Research*, *112*, A07220. https://doi.org/10.1029/2007JA012300

Gamayunov, K. V., Min, K., Saikin, A. A., & Rassoul, H. (2018). Generation of EMIC waves observed by Van Allen Probes at low L shells. *Journal of Geophysical Research: Space Physics*, *123*, 853–856. https://doi.org/10.1029/2018JA025629

Ge, Y. S., Raeder, J., Angelopoulos, V., Gilson, M. L., & Runov, A. (2011). Interaction of dipolarization fronts within multiple bursty bulk flows in global MHD simulations of a substorm on 27 February 2009. *Journal of Geophysical Research*, *116*, A00I23. https://doi.org/10.1029/2010JA015758

Golden, D. I., Spasojevic, M., Li, W., & Nishimura, Y. (2012). An empirical model of magnetospheric chorus amplitude using solar wind and geomagnetic indices. *Journal of Geophysical Research*, *117*, A12204. https://doi.org/10.1029/2012JA018210

Gonzalez, W. D., Tsurutani, B. T., Gonzalez, A. L. C., Smith, E. J., Tang, F., & Akasofu, S.-I. (1989). Solar wind-magnetosphere coupling during intense magnetic storms (1978 - 1979). *Journal of Geophysical Research*, *94*, 8835.

Groth, C. P. T., DeZeeuw, D. L., Gombosi, T. I., & Powell, K. G. (2000). Global three-dimensional MHD simulation of a space weather event: CME formation, interplanetary propagation, and interaction with the magnetosphere. *Journal of Geophysical Research*, *105*(A11), 25053.

Halford, A. J., Fraser, B. J., & Morley, S. K. (2010). EMIC wave activity during geomagnetic storm and nonstorm periods: CRRES results. *Journal of Geophysical Research*, *115*, A12248. https://doi.org/10.1029/2010JA015716

Hudson, M. K., Paral, J., Kress, B. T., Wiltberger, M., Baker, D. N., Foster, J. C., et al. (2015). Modeling CME-shock driven storms in 2012–2013: MHD-test particle simulations. *Journal of Geophysical Research: Space Physics*, *120*, 1168–1181. https://doi.org/10.1002/2014JA020833

Kennel, C. F., & Petschek, H. E. (1996). Limit on stably trapped particle fluxes. *Journal of Geophysical Research*, *71*, 1.

Kessel, R. L., Fox, N. J., & Weiss, N. (2013). The Radiation Belt Storm Probes (RBSP) and space weather. *Space Science Reviews*, *179*, 531–543. https://doi.org/10.1007/s11214-012-9953-6

Khazanov, G. V., Gamayunov, K. V., & Jordanova, V. K. (2003). Self-consistent model of magnetospheric ring current and electromagnetic ion cyclotron waves: The 2–7 May 1998 storm. *Journal of Geophysical Research*, *108*(A12), 1419. https://doi.org/10.1029/2003JA009856

Kivelson, M. G., & Pu, Z.-Y. (1984). The Kelvin-Helmholtz instability on the magnetopause. *Planetary and Space Science*, *32*(11), 1335.

Kletzing, C. A., Kurth, W. S., Acuna, M., MacDowall, R. J., Torbert, R. B., Averkamp, T., et al. (2013). The Electric and Magnetic Field Instrument Suite and Integrated Science (EMFISIS) on RBSP. *Space Science Reviews*, *179*, 127–181. https://doi.org/10.1007/S11214-013-9993-6

Lorentzen, K. R., McCarthy, M. P., Parks, G. K., Foat, J. E., Millan, R. M., Smith, D. M., et al. (2000). Precipitation of relativistic electrons by interaction with electromagnetic ion cyclotron waves. *Journal of Geophysical Research*, *105*, 5381.

Mauk, B. H., Fox, N. J., Kanekal, S. G., Kessel, R. L., Sibeck, D. G., & Ukhorskiy, A. (2013). Science objectives and rationale for the Radiation Belt Storm Probes Mission. *Space Science Reviews*, *179*, 3–27. https://doi.org/10.1007/s11214-012-9908-y

McCollough, J. P., Elkington, S. R., & Baker, D. N. (2009). Modeling EMIC wave growth during the compression event of 29 June 2007. *Geophysical Research Letters*, *36*, L18108. https://doi.org/10.1029/2009GL039985

McCollough, J. P., Elkington, S. R., Usanova, M. E., Mann, I. R., Baker, D. N., & Kale, Z. C. (2010). Physical mechanisms of compressional EMIC wave growth. *Journal of Geophysical Research*, *115*, A10214. https://doi.org/10.1029/2010JA015393

Min, K., Lee, J., Keika, K., & Li, W. (2012). Global distribution of EMIC waves derived from THEMIS observations. *Journal of Geophysical Research*, *117*, A05219. https://doi.org/10.1029/2012JA017515

Mourenas, D., Artemyev, A. V., Ma, Q., Agapitov, O. V., & Li, W. (2016). Fast dropouts of multi-MeV electrons due to combined effects of EMIC and whistler mode waves. *Geophysical Research Letters*, *43*, 415–416. https://doi.org/10.1002/2016GL068921

Ogawa, Y., Seki, K., Keika, K., & Ebihara, Y. (2019). Characteristics of CME- and CIR-driven ion upflows in the polar ionosphere. *Journal of Geophysical Research: Space Physics*, *124*, 3637–3649. https://doi.org/1029/2018JA025870

Park, J.-S., Kim, K.-H., Shiokawa, K., Lee, D.-H., Lee, E., Kwon, H.-J., et al. (2016). EMIC waves observed at geosynchronous orbit under quiet geomagnetic conditions ($Kp \leq 1$). *Journal of Geophysical Research: Space Physics*, *121*, 1377–1390. https://doi.org/10.1002/2015JA021968

Ridley, A. J., Lu, G., Clauer, C. R., & Papitashvili, V. O. (1997). Ionospheric convection during nonsteady interplanetary magnetic field conditions. *Journal of Geophysical Research*, *102*, 14563.

Roederer, J. G. (1970). *Dynamics of geomagnetically trapped radiation*. Berlin: Springer.

Russell, C. T., & McPherron, R. L. (1973). The magnetotail and substorms. *Space Science Reviews*, *15*, 205.

Saikin, A. A., Zhang, J.-C., Allen, R. C., Smith, C. W., Kistler, L. M., Spence, H. E., et al. (2015). The occurrence and wave properties of H^+-, He^+-, and O^+-band EMIC waves observed by the Van Allen Probes. *Journal of Geophysical Research: Space Physics*, *120*, 7477–7492. https://doi.org/10.1002/2015JA021358

Saikin, A. A., Zhang, J.-C., Smith, C. W., Spence, H. E., Torbert, R. B., & Kletzing, C. A. (2016). The dependence on geomagnetic conditions and solar wind dynamic pressure of the spatial distributions of EMIC waves observed by the Van Allen Probes. *Journal of Geophysical Research: Space Physics*, *121*, 4362–4377. https://doi.org/10.1002/2016JA022523

Sandanger, M., Soraas, F., Aarsnes, K., Oksavik, K., & Evans, D. S. (2007). Loss of relativistic electrons: Evidence for pitch angle scattering by electromagnetic ion cyclotron waves excited by unstable ring current protons. *Journal of Geophysical Research*, *112*, A12213. https://doi.org/10.1029/2006JA012138

Saunders, M. A., Freeman, M. P., Southwood, D. J., Cowley, S. W. H., Lockwood, M., Samson, J. C., et al. (1992). Dayside ionospheric convection changes in response to long-period interplanetary magnetic field oscillations: Determination of the ionospheric phase velocity. *Journal of Geophysical Research*, *97*, 19373.

Shen, X.-C., Hudson, M. K., Jaynes, A. N., Shi, Q., Tian, A., Claudepierre, S. G., et al. (2017). Statistical study of the storm time radiation belt evolution during Van Allen Probes era: CME- versus CIR-driven storms. *Journal of Geophysical Research: Space Physics*, *122*, 8327–8339. https://doi.org/10.1002/2017JA024100

Sibeck, D. G., Baumjohann, W., Elphic, R. C., Fairfield, D. H., & Fennell, J. F. (1989). The magnetospheric response to 8-minute period strong-amplitude upstream pressure variations. *Journal of Geophysical Research*, *94*, 2505.

Sibeck, D. G., Lopez, R. E., & Baumjohann, W. (1989). Solar wind dynamic pressure variations and transient magnetospheric signatures. *Geophysical Research Letters*, *16*, 13.

Tetrick, S. S., Engebretson, M. J., Posch, J. L., Olson, C. N., Smith, C. W., Denton, R. E., et al. (2017). Location of intense electromagnetic ion cyclotron (EMIC) wave events relative to the plasmapause: Van Allen Probes observations. *Journal of Geophysical Research: Space Physics*, *122*, 406–408. https://doi.org/10.1002/2016JA023392

Thorne, R., & Horne, R. (1994). Energy transfer between energetic ring current H^+ and O^+ by electromagnetic ion cyclotron waves. *Journal of Geophysical Research*, *99*, 17275.

Thorne, R., & Horne, R. (1997). Modulation of electromagnetic ion cyclotron instability due to interaction with ring current O^+ during magnetic storms. *Journal of Geophysical Research*, *102*, 14155.

Trattner, K. J., Fuselier, S. A., & Petrinec, S. M. (2004). Location of the reconnection line for northward interplanetary magnetic field. *Journal of Geophysical Research*, *109*, A03219. https://doi.org/10.1029/2003JA009975

Tsurutani, B. T., & Gonzalez, W. D. (1997). The interplanetary causes of magnetic storms: A review. In B. T. Tsurutani, W. D. Gonzalez, Y. Kamide, & J. K. Arballo (Eds.), *Magnetic storms* (Vol. 98, pp. 77). Washington, DC: American Geophysical Union.

Tsurutani, B. T., Gonzalez, W. D., Gonzalez, A. L. C., Tang, F., Arballo, J. K., & Okada, M. (1995). Interplanetary origin of geomagnetic activity in the declining phase of the solar cycle. *Journal of Geophysical Research*, *100*(A11), 21717.

Usanova, M. E., Mann, I. R., Bortnik, J., Shao, L., & Angelopoulos, V. (2012). THEMIS observations of electromagnetic ion cyclotron wave occurrence: Dependence on AE, SYMH, and solar wind dynamic pressure. *Journal of Geophysical Research*, *117*, A10218. https://doi.org/10.1029/2012JA018049

Wanliss, J. A., & Showalter, K. M. (2006). High-resolution global storm index: Dst versus SYM-H. *Journal of Geophysical Research*, *111*, A02202. https://doi.org/10.1029/2005JA011034

Wiltberger, M. J., Merkin, V., Lyon, J. G., & Ohtani, S. (2015). High-resolution global magnetohydrodynamic simulation of bursty bulk flows. *Journal of Geophysical Research: Space Physics*, *120*, 4555–4566. https://doi.org/10.1002/2015JA021080

Wygant, J., Rowland, D., Singer, H. J., Temerin, M., Mozer, F., & Hudson, M. K. (1998). Experimental evidence on the role of the large spatial scale electric field in creating the ring current. *Journal of Geophysical Research*, *103*(A12), 29527.